JCTC Journal of Chemical Theory and Computation

pubs.acs.org/JCTC Article

Nonadiabatic Molecular Dynamics with Extended Density Functional Tight-Binding: Application to Nanocrystals and Periodic Solids

Mohammad Shakiba, Elizabeth Stippell, Wei Li, and Alexey V. Akimov*

Cite This: J. Chem. Theory Comput. 2022, 18, 5157−5180 Read Online

ACCESS | Metrics & More | Article Recommendations | Supporting Information

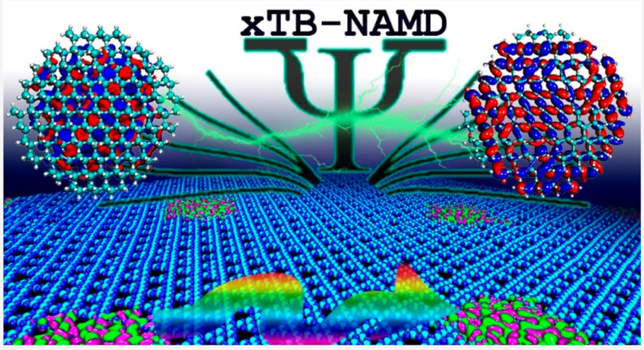

ABSTRACT: In this work, we report a new methodology for nonadiabatic molecular dynamics calculations within the extended tight-binding (xTB) framework. We demonstrate the applicability of the developed approach to finite and periodic systems with thousands of atoms by modeling "hot" electron relaxation dynamics in silicon nanocrystals and electron−hole recombination in both a graphitic carbon nitride monolayer and a titanium-based metal−organic framework (MOF). This work reports the non-adiabatic dynamic simulations in the largest Si nanocrystals studied so far by the xTB framework, with diameters up to 3.5 nm. For silicon nanocrystals, we find a non-monotonic dependence of "hot" electron relaxation rates on the nanocrystal size, in agreement with available experimental reports. We rationalize this relationship by a combination of decreasing nonadiabatic couplings related to system size and the increase of available coherent transfer pathways in systems with higher densities of states. We emphasize the importance of proper treatment of coherences for obtaining such non-monotonic dependences. We characterize the electron−hole recombination dynamics in the graphitic carbon nitride monolayer and the Ti-containing MOF. We demonstrate the importance of spin-adaptation and proper sampling of surface hopping trajectories in modeling such processes. We also assess several trajectory surface hopping schemes and highlight their distinct qualitative behavior in modeling the excited-state dynamics in superexchange-like models depending on how they handle coherences between nearly parallel states.

1. INTRODUCTION

Nonadiabatic molecular dynamics (NA-MD) is a powerful computational technique that can model NA processes and describe the excited-state dynamics in various materials. NA-MD simulations have been successfully utilized in predicting the photochemistry and photophysics of molecular systems[1−9] and nanoscale materials.[10−36] These simulations have been widely used to gain insights into NA processes in solar cells,[10−31] light-emitting diodes,[32] and chemical reactions.[33−36] However, due to the highly demanding computational costs, the NA-MD simulations of solid-state and nanoscale systems are often limited to a few hundred atoms. Simulation of realistic nanostructures, comparable to those studied experimentally is still computationally expensive, primarily due to the demanding costs of the underlying electronic structure calculations and their unfavorable scalability with the system size. Density functional theory (DFT)-based approaches have been widely adopted for simulation of small- and medium-sized systems[37−39] but are still unfeasible for modeling large nanostructures. Alternative methods leveraged the use of density functional tight-binding (DFTB),[40−45] semiempirical,[46−51] or hybrid quantum mechanical/molecular mechanics[52,53] approaches. Several fragment-based schemes[44,45,54−61] and vibronic coupling methods[62] were developed to improve the scalability of the methods. Alternatively, NAC-free approaches[28,63−65] have been explored as a route to inexpensive NA-MD simulations. Their applicability to nanoscale systems was reported recently.[28]

The linear-scaling techniques are indispensable to extremely large systems; however, in several thousand atom systems, the pre-factor in the timing may be rather large. This motivates us to further explore the applicability of the fast DFTB or semiempirical methods to modeling NA-MD in extended systems. Although the DFTB approach has been successful in modeling many bio and organic structures,[66−70] including modeling NA dynamics,[44,45,71] its parameterization is limited for inorganic systems, rendering many inorganic materials of

Received: March 26, 2022
Published: June 27, 2022

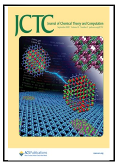

https://doi.org/10.1021/acs.jctc.2c00297
J. Chem. Theory Comput. 2022, 18, 5157−5180

interest to solar cell harvesting out of its scope. Recently, Bannwarth et al.[72−74] proposed the extended tight-binding (xTB) method as a novel TB approach for simulating systems up to few thousands of atoms. In this method, the DFT Hamiltonian is expanded to the third order in charge density perturbation relative to the reference value followed by several other approximations to model electrostatic interactions and exchange−correlation effects. The xTB method has an extended parameterization to describe the geometry, vibrational frequencies, and non-covalent interactions of systems with element numbers $Z = 1-86$. Thus, the xTB approach is a promising foundation for modeling NA processes in diverse inorganic materials, for which the DFTB parameterization may not be available. The xTB approach is implemented in various packages, such as CP2K,[75,76] DFTB+,[42,43] ORCA,[77] TeraChem,[78] and TURBOMOLE.[79] It has been successfully applied to model metal−organic frameworks,[80,81] large-scale bio[82] and organic[83,84] structures to name a few. However, the applicability of the xTB to model NA processes has not been explored yet.

In this work, we report the development of a new methodology for NA-MD simulations within the framework of xTB electronic structure calculations (xTB/NA-MD). Apart from leveraging the significantly cheaper electronic structure calculations, we implement an improved procedure for computing NA couplings (NACs) between pairs of excited states. Previously, we implemented a methodology to compute the required integrals using the Gaussian "cube" files.[29,30,85] The "cube" approach has also been utilized by others.[86] Although such a grid-based integration method can be used with different types of basis sets and is easy to implement, it can demand a significant amount of disk-space. Storing a single wavefunction in a "cube" file may require gigabytes of memory; therefore, doing this task for hundreds of states and thousands of steps is impractical for large systems. However, another elegant approach adopted in some codes, such as Newton-X[4] and SHARC,[87] includes computing the AO time−overlap integrals by requesting the electronic structure codes to produce the integrals for auxiliary double-molecule systems, in which the molecular geometries at two nearby time intervals t and $t + \Delta t$ are superimposed.[88] Although quite robust and easy to implement, such an approach depends on the availability of infrastructure and functionality in the electronic structure codes. In addition, it is not optimal because such a program also computes the overlaps within the systems, at least doubling the computational time.

As an alternative to the prior approaches, in this work, we have directly integrated Libra[89] with the Libint2 library[90] for computing the required time−overlap integrals analytically. Such calculations compute only what is needed in the NA-MD workflow, can take advantage of the OpenMP parallelization, and require only a lightweight representation of AO basis of extended systems (e.g., molden format). In addition, the availability of the analytical procedures enable us to use the resulting integrals in the context of periodic calculations. The super-molecule approach may not be suitable in this situation. Furthermore, we leverage the use of sparse representation formats for storing the desired time−overlap and NAC matrices for systems with hundreds of states.

We demonstrate how the developed methodology can be used to model excited-state dynamics in unprecedentedly large Si nanocrystals (NCs), as well as in periodic solids, such as a graphitic carbon nitride monolayer and a titanium-based metal−organic framework (MOF). In the last decade, colloidal NCs have demonstrated their potential to replace the forerunner silicon solar cells that work similarly to dye-sensitized solar cells while having flexibility in production with size-tunable optoelectronic properties due to their quantum confinement properties.[91−93] Among them, silicon NCs (Si NCs) are of particular interest due to lack of their toxicity, the element's pre-existing prevalence in the electronic industry, and its natural abundance.[94−96] Our second system of interest, the graphitic carbon nitride monolayer, has recently attracted a lot of interest as a material for photocatalytic applications such as solar-driven water splitting.[97−99] The third system is the MIL-125-NH_2 MOF, which is based on titanium and has different photovoltaic and photocatalytic applications such as in CO_2 reduction.[100−103] In this work, we assess the quality of electronic structure and NACs as computed using the xTB, the GFN2 parametrization,[73] and DFT methods. We assess the new scheme for computing NACs that utilizes the Libint2 library for analytical computation of time−overlap integrals. We validate the new scheme against the numerical integration approach developed previously. Finally, we discuss the general applicability of the xTB-based NA-MD to modeling NA processes in extended systems. Various trajectory-surface hopping (TSH) and decoherence schemes are also assessed.

2. THEORY AND METHODS

2.1. Nonadiabatic Molecular Dynamics. The overall NA-MD approach adopted here is similar to the one used in our prior works.[29,30] The detailed description of the algorithms and their analysis can be found in those works and in several reviews.[50,104−107] Here, we only briefly outline the key components of the used methodology.

The quantum dynamics of electronic degrees of freedom is described by the time-dependent Schrodinger equation (TD-SE)

$$i\hbar\frac{\partial\Psi(r, R, t)}{\partial t} = \hat{H}(r, R, t)\Psi(r, R, t) \tag{1}$$

where r and R are coordinates of electrons and nuclei, respectively. $\hat{H} = \hat{T} + \hat{H}_{\text{el}}$ is the system's Hamiltonian, $\hat{T}$ is the nuclear kinetic energy operator, and $\hat{H}_{\text{el}}$ is the electronic Hamiltonian. Within the quantum-classical approach,[108] the TD-SE solution is given in terms of the Born−Huang-like ansatz

$$\Psi(r, R, t) = \sum_i c_i(t)\Phi_i(t, r; R(t)) \tag{2}$$

Here, $\Phi_i(t,r;R(t))$ is the ith adiabatic electronic wavefunction, parametrically dependent on nuclear trajectories, $R(t)$, and $c_i(t)$ are the amplitudes of the coherent superposition (also referred to as "coherent amplitudes" for simplicity). These amplitudes act as effective electronic degrees of freedom, while nuclear coordinates and momenta are treated classically and their evolution follows the classical Hamiltonian equations of motion on the corresponding active potential energy surfaces.

The evolution of electronic amplitudes is given by the simplified version of the TDSE

$$i\hbar\dot{c}_i(t) = \sum_j H_{vib,ij}(t)c_j(t) \tag{3}$$

$$H_{vib,ij}(t) = E_j(R(t))\delta_{ij} - i\hbar d_{ij}^{(1)}(R(t)) \tag{4}$$

Here, $E_j(R(t))$ is the adiabatic energy and $d_{ij}^{(1)}$ is the scalar or time-derivative NAC

$$d_{ij}^{(1)} = \langle \Phi_i(t, r; R(t))|\frac{\partial}{\partial t}|\Phi_j(t, r; R(t))\rangle \tag{5}$$

Furthermore, in this work, we adopt the neglect of back-reaction approximation (NBRA) pioneered by Prezhdo et al.[109−111] and further adopted by many researchers modeling NA dynamics in nanoscale systems.[10−36] According to the NBRA, the electronic evolution does not affect the nuclear evolution, whereas the latter (on the ground electronic state) parametrically affects the corresponding vibronic Hamiltonian. This approach cannot properly describe the thermal equilibrium because it does not take the derivative couplings into account and there is no feedback between quantum and classical parts of the system. In the NBRA model, the nuclear velocities are not rescaled upon the acceptance of any hop (up or down in energy level) as in the original Tully's fewest switch surface hopping (FSSH)[108] scheme. Thus, the total energy of the system is not conserved, which can be regarded as an implicit coupling to the environment, causing dissipative dynamics. This approach is mostly suitable for nanoscale systems where the computation of the derivative coupling vectors is not feasible but previous studies reported that in bulk semiconductors, the NBRA may break down in DFTB-based surface hopping simulations due to a strong dependence of the nuclear motion on the electronic states.[112] Also, a previous study has shown that the FSSH may fail when too many states are present in the dynamics.[113] In the present work, we adopt the NBRA approach for NA-MD simulations of excited states and assess its applicability to hot-electron relaxation and electron−hole recombination dynamics.

The time-dependent coherent amplitudes are used next as to define one of the surface hopping approaches. According to the FSSH method,[108] a trajectory in state i can stochastically hop to state j with the hopping probability

$$P_{i\to j}^{\text{prop}}(t, t + \Delta t) = \max\left(0, \frac{\Delta t}{\rho_{ii}}\text{Im}[\rho_{ij}H_{vib,ji} - H_{vib,ij}\rho_{ji}]\right) \tag{6}$$

where

$$\rho_{ij} = c_i c_j^* \tag{7}$$

Because the current approach follows the NBRA, the frustrated hops are treated using the proposed-hop acceptance probabilities

$$P_{i\to j}^{\text{acc}} = \min\left(1, \exp\left(-\frac{E_j - E_i}{k_B T}\right)\right), \qquad i \neq j \tag{8}$$

In this work, we also consider several decoherence approaches: (a) the instantaneous decoherence at attempted hops (ID-A) of Nelson and Tretiak,[114] (b) the modified version of the simplified decay of mixing (mSDM) of Smith and Akimov[115] based on the original SDM method of Granucci and Persico,[116] and (c) the decoherence-induced surface hopping (DISH) algorithm of Jaeger and Prezhdo.[117,118]

The ID-A and mSDM techniques can be considered as relatively simple add-ons on top of the base NBRA-FSSH algorithm outlined above. These techniques simply modify the coherent amplitudes, c_i, as follows. In the ID-A, the amplitudes are reset at every attempted hop ($\xi < P_{i\to j}^{\text{prop}}$, $\xi \in U[0,1]$) as

$$c_j^{\text{new}} = \frac{c_j^{\text{old}}}{|c_j^{\text{old}}|}, \qquad c_i^{\text{new}} = 0, \ \forall\ i \neq j \tag{9}$$

In the mSDM method, the coherent amplitudes are modified at every time-step, exactly as in the SDM approach of Granucci and Persico[116]

$$c_i^{\text{new}} = c_i^{\text{old}} \exp\left(-\frac{\Delta t}{\tau_{if}}\right), \qquad \forall\ i \neq f \tag{10a}$$

$$c_f^{\text{new}} = c_f^{\text{old}}\sqrt{\frac{1 - \sum_{i\neq f}|C_i^{\text{new}}|^2}{|C_f^{\text{old}}|^2}} \tag{10b}$$

The main distinction with the SDM approach is the definition of the parameters τ_{ij}. Specifically, we define them as the dephasing rates given earlier by Akimov and Prezhdo[119]

$$\tau_{ij}^{-1} = \sqrt{\frac{5\delta E_{ij}^2}{12\hbar^2}} \tag{11}$$

Here, $\langle \delta E_{ij}^2\rangle$ is the fluctuation of the energy gap, $\langle \delta E_{ij}^2\rangle = \langle(\Delta E_{ij} - \langle\Delta E_{ij}\rangle)^2\rangle$, where $\Delta E_{ij} = E_i - E_j$ and $\langle * \rangle$ denotes the ensemble- and trajectory averaging.

The DISH algorithm is implemented according to the prescription given by Jaeger and Prezhdo[117] with the revisions discussed recently by one of us.[118] In summary, the surface hops are determined by the Poisson process sampling the "decoherence events". The times of such events are sampled from the exponential distribution with a characteristic timescale given by the one-state decoherence time

$$\tau_i^{-1} = \sum_{j\neq i} \rho_{jj}\tau_{ij}^{-1} \tag{12}$$

The τ_{ij} parameters are computed according to eq 11. If the decoherence event is determined for a state i, the hop to a new state j is attempted with the probability given by the quantum population of the target state, $P_{i\to j}^{\text{prop}} = \rho_{jj}$. If the hop is accepted based on eq 8, the superposition is collapsed onto the new state; this state becomes the active one. If the proposed hop is not accepted, the corresponding state is projected out from the coherent superposition and no hop occurs. If the decoherence event is determined for a subset of states at a given time step, the above operation is applied to each of the states in the subset randomly, until either the collapse on one of the states occurs or all states in the subset are projected out. A more detailed description of various situations that can arise in this algorithm is given in a recent revision of the DISH algorithm.[118]

2.2. Computing Nonadiabatic Couplings and Time−Overlap Matrices. The formulation and implementation of the procedures to compute NACs, eq 5, and time−overlap matrix elements is one of the key components in this work. The calculation of NAC, eq 5, is based on the time−overlap formula of Hammes−Schiffer and Tully[120]

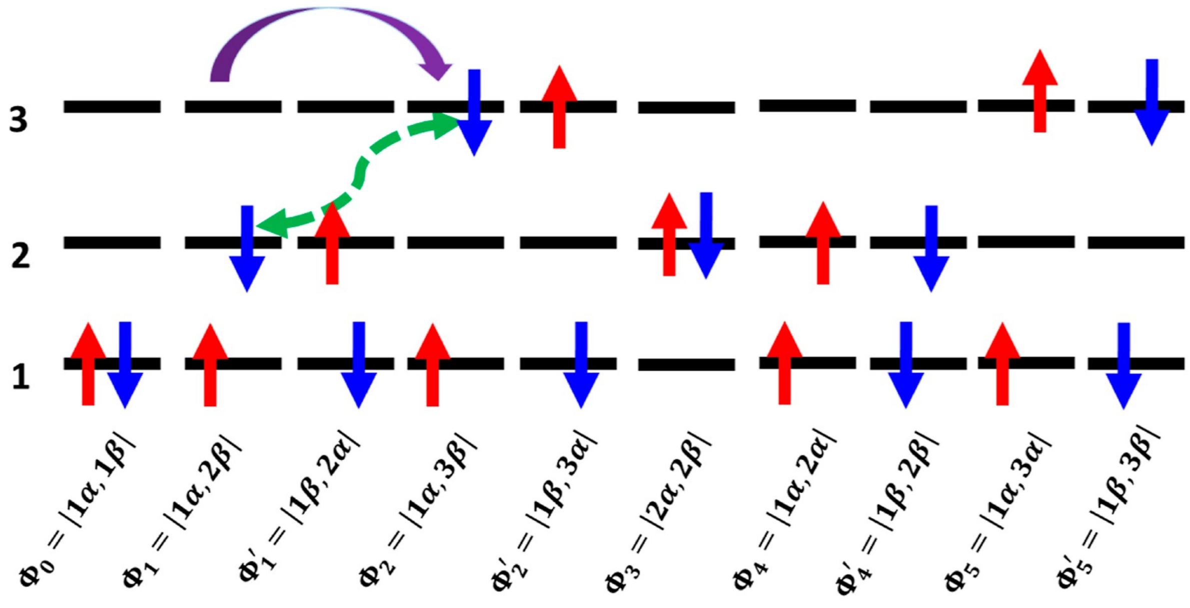

(a)

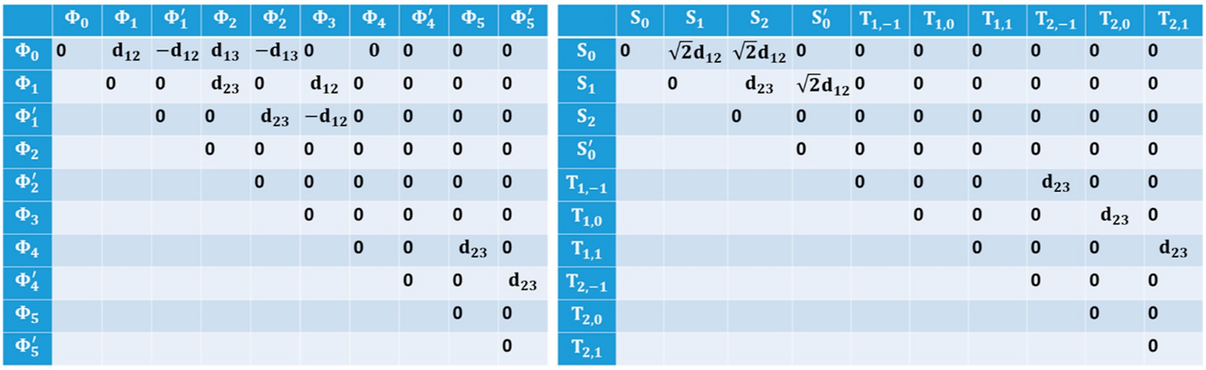

	Φ_0	Φ_1	Φ_1'	Φ_2	Φ_2'	Φ_3	Φ_4	Φ_4'	Φ_5	Φ_5'
Φ_0	0	d_{12}	$-d_{12}$	d_{13}	$-d_{13}$	0	0	0	0	0
Φ_1		0	0	d_{23}	0	d_{12}	0	0	0	0
Φ_1'			0	0	d_{23}	$-d_{12}$	0	0	0	0
Φ_2				0	0	0	0	0	0	0
Φ_2'					0	0	0	0	0	0
Φ_3						0	0	0	0	0
Φ_4							0	0	d_{23}	0
Φ_4'								0	0	d_{23}
Φ_5									0	0
Φ_5'										0

(b)

	S_0	S_1	S_2	S_0'	$T_{1,-1}$	$T_{1,0}$	$T_{1,1}$	$T_{2,-1}$	$T_{2,0}$	$T_{2,1}$
S_0	0	$\sqrt{2}d_{12}$	$\sqrt{2}d_{12}$	0	0	0	0	0	0	0
S_1		0	d_{23}	$\sqrt{2}d_{12}$	0	0	0	0	0	0
S_2			0	0	0	0	0	0	0	0
S_0'				0	0	0	0	0	0	0
$T_{1,-1}$					0	0	0	d_{23}	0	0
$T_{1,0}$						0	0	0	d_{23}	0
$T_{1,1}$							0	0	0	d_{23}
$T_{2,-1}$								0	0	0
$T_{2,0}$									0	0
$T_{2,1}$										0

(c)

Figure 1. Schematic representation of (a) single-particle SD basis. The evaluated NAC are shown for (b) SD and (c) SAC states.

$$d_{ij}\left(t + \frac{\Delta t}{2}\right) \approx \frac{\langle \Phi_i(t)|\Phi_j(t + \Delta t)\rangle - \langle \Phi_i(t + \Delta t)|\Phi_j(t)\rangle}{2\Delta t}$$

$$= \frac{\langle \Phi_i(t)|\Phi_j(t + \Delta t)\rangle - (\langle \Phi_j(t)|\Phi_i(t + \Delta t)\rangle)^*}{2\Delta t}$$

$$= \frac{St_{ij} - (St_{ji})^*}{2\Delta t} \tag{13}$$

Or in a matrix form

$$D = \frac{1}{2\Delta t}(St - St^+) \tag{14}$$

The choice of the electronic basis functions, $\{\Phi_i\}$, deserves a separate discussion. In many prior works on NA-MD simulations, such functions are chosen as either KS or MO orbitals,[31,37,106,121−124] or as the Slater determinants (SDs).[25,28−30,69,125−127] Although the adoption of the SD basis has been helpful in enabling modeling coupled electron−nuclear dynamics, for example, in Auger processes, such functions still miss an important physical constraint of being the eigenfunctions of the spin operator $\hat{S}^2$. A proper solution is the use of the spin-adapted configurations (SACs). In this work, we for the first time explicitly introduce SAC dynamical functions in the context of NBRA-based NA-MD calculations. We are interested only in the close-shell and open-shell spin-singlet SACs, such as those present in various excited configurations

$$\Phi_{ij}^{\mathrm{SAC}} = \frac{1}{\sqrt{2}}(\Phi_{ij} - \Phi_{j'}) \tag{15a}$$

Here, i and j indicate the singly occupied spin-orbitals that constitute the open shell. The primes indicate the spin flip of the corresponding spin-orbitals. For instance, if $i = \phi_1\alpha$, then i'

$= \phi_1\beta$. Note that the closed-shell configurations are already the eigenfunctions of the $\hat{S}^2$ operator, so the SAC is trivially a SD

$$\Phi_{ij}^{\mathrm{SAC}} = \Phi_{ij}^{\mathrm{SD}} \tag{15b}$$

In this case, i and j correspond to the same spatial orbital but have opposite spin components.

Computing St^{SAC} to be used in eqs 13 or 14 can be regarded as a linear transformation of St^{SD}. Here, $St_{ij}^{\mathrm{SD}} = \langle \Phi_i(t)|\Phi_j(t + \Delta t)\rangle$ is the matrix element of the time−overlap matrix St in the basis of excited SDs, $\{\Phi_i\}$, included in the dynamical basis of the problem. The time−overlaps of the SDs can be computed according to the Lowdin formula

$$\begin{aligned} St_{ij}^{\mathrm{SD}} &= \langle \Phi_i(t)|\Phi_j(t + \Delta t)\rangle = \\ &\left\langle \frac{1}{\sqrt{N!}}|\psi_{i,1}(t)\psi_{i,2}(t)...\psi_{i,N}(t)| \middle| \frac{1}{\sqrt{N!}}|\psi_{j,1}(t + \Delta t)\psi_{j,2}(t + \Delta t)...\psi_{j,N}(t + \Delta t)| \right\rangle = \\ &\det \begin{vmatrix} \langle \psi_{i,1}(t)|\psi_{j,1}(t + \Delta t)\rangle & \langle \psi_{i,1}(t)|\psi_{j,2}(t + \Delta t)\rangle & ... & \langle \psi_{i,1}(t)|\psi_{j,N}(t + \Delta t)\rangle \\ \langle \psi_{i,2}(t)|\psi_{j,1}(t + \Delta t)\rangle & \langle \psi_{i,2}(t)|\psi_{j,2}(t + \Delta t)\rangle & ... & \langle \psi_{i,2}(t)|\psi_{j,N}(t + \Delta t)\rangle \\ \langle \psi_{i,N}(t)|\psi_{j,1}(t + \Delta t)\rangle & \langle \psi_{i,N}(t)|\psi_{j,2}(t + \Delta t)\rangle & ... & \langle \psi_{i,N}(t)|\psi_{j,N}(t + \Delta t)\rangle \end{vmatrix} \end{aligned} \tag{16}$$

Here, $\psi_{i,j}$ is the jth spin−orbital occupied in the ith SD. The computation of the time−overlaps of the xTB Kohn−Sham (KS) orbitals, $St_{ab}^{\mathrm{KS}} = \langle \psi_a(t)|\psi_b(t + \Delta t)\rangle$, is based on the transformation of the corresponding atomic orbitals

$$St^{\mathrm{KS}} = U^{+}(t)St^{\mathrm{AO}}U(t + \Delta t) \tag{17}$$

$$\psi_i^{\mathrm{KS}}(t) = \sum_j U_{ji}(t)\phi_j^{\mathrm{AO}}(t) \tag{18}$$

Here, ψ_i^{KS} are the KS orbitals, whereas ϕ_j^{AO} are the atomic orbitals. The matrices U contain the amplitudes of the AOs in the corresponding KS orbitals.

However, as has been demonstrated earlier by Akimov and Prezhdo[125,126] and later generalized by Ryabinkin and Izmaylov,[128,129] the calculations of the NACs according to eqs 13 or 14 in the SD basis can be significantly simplified and reduced to computing the NACs in the KS (or orbital basis). Namely, if two SDs, Φ_I and Φ_J differ by the occupation of the orbitals ϕ_i and ϕ_j only, the couplings in the SD and orbital bases are related

$$D_{IJ}^{\mathrm{SD}} = d_{ij}^{\mathrm{KS}} \tag{19}$$

A schematic representation of such a relationship is shown in Figure 1a. Here, the NAC between SDs Φ_1 and Φ_2 is given by the NAC between changed orbitals 2 and 3, that is $D_{\Phi1\Phi2} = d_{23}$. Here, d_{ij}^{KS} is computed according to eqs 13 or 14 using time−overlaps from eq 17. The full set of possible determinant types needed to represent singlet and triplet configurations is given in Figure 1b with the derivations of the corresponding matrix elements detailed in Section S1 of the Supporting Information.

Finally, the NACs in the SD basis (Figure 1b) can be transformed into the basis of the corresponding SACs (Figure 1c), as detailed in Section S1 of the Supporting Information. The main non-trivial result from such derivations is that the NACs between the proper SACs of the closed-shell type (e.g., S_0) and the open-shell type (either S_1 or S_2) gains an additional factor of $\sqrt{2}$ in comparison to the NAC in the corresponding SD basis. It is likely that such a correction might have been present in works that utilize NACs returned by the electronic structure packages (e.g., those with Newton-X or SHARC codes). However, the type of correction was never explicitly discussed in the prior NA-MD works of electron−hole recombination modeled within the NBRA approach. The present work explicitly introduces it in the context of such simulations for the first time.

At the same time, we find that the coupling between two distinct SAC of the open-shell type does still reduce the coupling of the corresponding orbitals (as long as there is only one pair of distinct occupied orbitals in the two SDs). For instance, $D_{S_1S_2} = D_{\Phi_1\Phi_2} = d_{23}$ (Figure 1, panels c and d). Thus, the processes such as hot electron or hot hole relaxation are not affected by the spin-adaptation and prior simulation of this kind is not compromised. However, prior results reporting the electron−hole recombination or other processes involving double-excited closed-shell configuration such as modeling of singlet fission or Auger processes may need a revision.

Finally, our derivations indicate that there is no nonadiabatic coupling between the components of the triplet with different m_s quantum numbers. This result is not relevant to the calculations presented in this work but would be useful when one models quantum transitions within the manifold of triplet states, such as in triplet energy-transfer simulations.

The calculations of time−overlaps in the KS basis, eq 17, require the time−overlaps in the atomic orbital (AO) basis. The latter are given as

$$St_{ab}^{\mathrm{AO}} = \langle \phi_a(t)|\phi_b(t + \Delta t)\rangle \tag{20}$$

In our prior developments, we utilized the cube file-based numerical integration to compute the St^{AO} matrix elements.[29,30] In the present work, we interfaced the Libra package with the Libint2 library for efficient computation of the underlying molecular integrals, as detailed in the following section. This development enables us to handle much larger systems considered in this work.

For periodic systems, KS orbitals (or more properly, crystal orbitals) are given in terms of corresponding Bloch functions, $\beta_{\mathbf{k},j}$

$$\psi_{\mathbf{k},i}^{\mathrm{KS}}(t) = \sum_j U_{\mathbf{k},ji}(t)\beta_{\mathbf{k},j}(t) \tag{21}$$

The Bloch function for a crystal momentum, $\mathbf{k}$, is defined using the localized AO functions, ϕ_a, as follows

$$\beta_{\mathbf{k},a}(\mathbf{r}) = \frac{1}{\sqrt{N}} \sum_{\mathbf{t}} \mathrm{e}^{i\mathbf{k}\mathbf{t}} \phi_a(\mathbf{r} - \mathbf{t}) \tag{22}$$

Here, the summation is over N translational vectors $\mathbf{t}$ relative to the central cell.

The overlap of two Bloch functions, $\beta_{\mathbf{k},a}(\mathbf{r})$ and $\beta_{\mathbf{k},b}(\mathbf{r})$, can be computed for general sets of $\mathbf{k}$ and band index, a, quantum numbers

$$\begin{aligned} St^{\mathrm{B}}_{\mathbf{k},a,\mathbf{k}',b} &= \langle \beta_{\mathbf{k},a}(t) | \beta_{\mathbf{k}',b}(t + \Delta t) \rangle \\ &= \frac{1}{N} \int \mathrm{d}\mathbf{r} \sum_{\mathbf{t},\mathbf{t}'} \mathrm{e}^{-i\mathbf{k}\mathbf{t}} \phi_a^*(\mathbf{r} - \mathbf{t}) \mathrm{e}^{i\mathbf{k}'\mathbf{t}'} \phi_b \\ (\mathbf{r} - \mathbf{t}') &= \frac{1}{N} \\ \sum_{\mathbf{t},\mathbf{t}'} \int \mathrm{d}\mathbf{r}\, & \mathrm{e}^{i(\mathbf{k}'\mathbf{t}' - \mathbf{k}\mathbf{t})} \phi_a^*(\mathbf{r} - \mathbf{t}, t) \phi_b(\mathbf{r} - \mathbf{t}', t + \Delta t) \end{aligned} \tag{23}$$

Now, if we set $\mathbf{R} = \mathbf{t}' - \mathbf{t}$

$$\begin{aligned} St^{\mathrm{B}}_{\mathbf{k},a,\mathbf{k}',b} &= \langle \beta_{\mathbf{k},a} | \beta_{\mathbf{k}',b} \rangle \\ &= \frac{1}{N} \sum_{\mathbf{t},\mathbf{t}'} \int \mathrm{d}\mathbf{r}\; \mathrm{e}^{i(\mathbf{k}'\mathbf{t}' - \mathbf{k}\mathbf{t})} \phi_a^*(\mathbf{r} - \mathbf{t}) \phi_b \\ (\mathbf{r} - \mathbf{t} - \mathbf{R}) &= \frac{1}{N} \\ \sum_{\mathbf{t},\mathbf{R}} \mathrm{e}^{i(\mathbf{k}'(\mathbf{t}+\mathbf{R}) - \mathbf{k}\mathbf{t})} & \int \mathrm{d}\mathbf{r}\; \phi_a^*(\mathbf{r} - \mathbf{t}) \phi_b(\mathbf{r} - \mathbf{t} - \mathbf{R}) = \\ \sum_{\mathbf{R}} \mathrm{e}^{i\mathbf{k}'\mathbf{R}} \frac{1}{N} \sum_{\mathbf{t}} & \mathrm{e}^{i(\mathbf{k}' - \mathbf{k})\mathbf{t}} \int \mathrm{d}\mathbf{r}\; \phi_a^*(\mathbf{r} - \mathbf{t}) \phi_b(\mathbf{r} - \mathbf{t} - \mathbf{R}) \end{aligned} \tag{24}$$

By setting $\mathbf{r}' = \mathbf{r} - \mathbf{t}$, $\mathrm{d}\mathbf{r}' = \mathrm{d}\mathbf{r}$, we recognize that the integral $\int \mathrm{d}\mathbf{r}\; \phi_a^*(\mathbf{r} - \mathbf{t}) \phi_b(\mathbf{r} - \mathbf{t} - \mathbf{R})$ can be simplified to the form that does not depend on the absolute translational vectors but only on the difference of the translational vectors with respect to each other, $\mathbf{R} = \mathbf{t}' - \mathbf{t}$

$$\begin{aligned} &\int \mathrm{d}\mathbf{r}\; \phi_a^*(\mathbf{r} - \mathbf{t}, t) \phi_b(\mathbf{r} - \mathbf{t} - \mathbf{R}, t + \Delta t) \\ &= \int \mathrm{d}\mathbf{r}'\; \phi_a^*(\mathbf{r}', t) \phi_b(\mathbf{r}' - \mathbf{R}, t + \Delta t) \\ &\equiv St^{\mathrm{AO}}_{ab}(\mathbf{R}) \end{aligned} \tag{25}$$

With this simplification, the overlap of the Bloch functions becomes

$$St^{\mathrm{B}}_{\mathbf{k},a,\mathbf{k}',b} = \langle \beta_{\mathbf{k},a} | \beta_{\mathbf{k}',b} \rangle = \sum_{\mathbf{R}} \mathrm{e}^{i\mathbf{k}'\mathbf{R}} \frac{1}{N} \sum_{\mathbf{t}} \mathrm{e}^{i(\mathbf{k}' - \mathbf{k})\mathbf{t}} St^{\mathrm{AO}}_{ab}(\mathbf{R}) \tag{26}$$

In this work, we consider a special case of single k-point calculations. Thus, $\mathbf{k} = \mathbf{k}'$, and the above expression simplifies to

$$St^{\mathrm{B}}_{\mathbf{k},a,\mathbf{k},b} = \langle \beta_{\mathbf{k},a} | \beta_{\mathbf{k},b} \rangle = \sum_{\mathbf{R}} \mathrm{e}^{i\mathbf{k}\mathbf{R}} S^{\mathrm{AO}}_{ab}(\mathbf{R}) \tag{27}$$

This formula has also been discussed in the implementation of the TB methods for periodic systems.[42] In the case of nonperiodic calculations, the overlap between Bloch functions is computed only for the central cell $\mathbf{R} = (0,0,0)$ and the time−overlap formula reduces to that of AOs

$$St^{\mathrm{B}}_{\mathbf{k},a,\mathbf{k},b} = \langle \beta_{\mathbf{k},a} | \beta_{\mathbf{k},b} \rangle = \langle \phi_a | \phi_b \rangle = St^{\mathrm{AO}}_{ab} \tag{28}$$

The time−overlap matrices in the SD basis can be used to track the identities of states via trivial crossing identification via the min-cost algorithm[130] as discussed elsewhere.[29] The identified trivial crossings can be reflected in the auxiliary time−overlap matrices, which are computed from the original ones by applying the corresponding cumulative permutations of rows and columns. However, in the current work, the state tracking was disabled for Si NC systems because the computations become rather expensive for systems with hundreds of states. Our prior experience with model systems shows that the trivial state crossing identification becomes rather negligible in dense manifolds of states.[131] The state tracking is included in modeling dynamics in both the graphitic C_3N_4 monolayer and MIL-125-NH_2 MOF. The corrected time−overlap matrices are used to compute the phase-correction[132] to ensure the dynamical consistency of the wavefunctions in all steps of the MD. The resulting corrected time−overlaps are used to compute NACs according to eq 13. Although the current work focuses on the single-particle description of the excited states, the developed Libint2-based frameworks for computing time−overlaps and NACs is general and can be used in DFT-based calculations or calculations involving TD-DFT states as demonstrated in our prior workflows.[29,30,118]

2.3. Implementation.

The described methodology is implemented within the Libra/CP2K interface modules of the Libra code v5.2.1.[133] We use the CP2K package[76] for electronic structure calculations at the xTB or (TD)DFT level of theory. The MO-LCAO coefficients for every nuclear geometry, $U(t)$, are saved by CP2K in either a "*MOLog*" or "*molden*"[134] file formats. We choose the "*molden*" file format because it contains not only all the MO coefficients and energies for each spin−orbital but also the structure coordinates and the basis set contraction coefficients and exponents for each angular momentum component. This information is parsed to Libra to compute the AO time−overlaps, St^{AO}, using Libint2 functions. The "*molden*" files are printed out at every time step of the CP2K-based MD and are used to compute the desired MO time−overlaps on-the-fly. The "*molden*" file format is not specific to xTB and can be used with other types of calculations in CP2K, such as DFT, but it cannot be used with DFTB because the basis set used by this methodology is of Slater-type orbitals, where CP2K analysis tools are based on Gaussian-type orbitals.

We utilize the Libint2.6 library for computing the time−overlap integrals in the AO basis. The Libint2 library functions are optimized to compute the integrals both in spherical and Cartesian coordinates. For fast and efficient computation of the MO overlaps, we split the equilibrated MD trajectory and perform the calculations in multiple jobs by setting up the electronic structure calculations for each of them simultaneously. Using this technique, one can significantly increase the speed of the calculations by leveraging multiple compute nodes if available.

In this work, we utilize CP2K versions 8.2 and 9.1. In CP2K, one can use a previously converged wavefunction, stored in a compressed binary "*wfn*" file, as the initial density guess in another calculation, including a slightly perturbed structure. This approach helps in reducing the computational time by decreasing the number of self-consistent field (SCF) cycles to achieve the convergence to a desired tolerance. Except for the

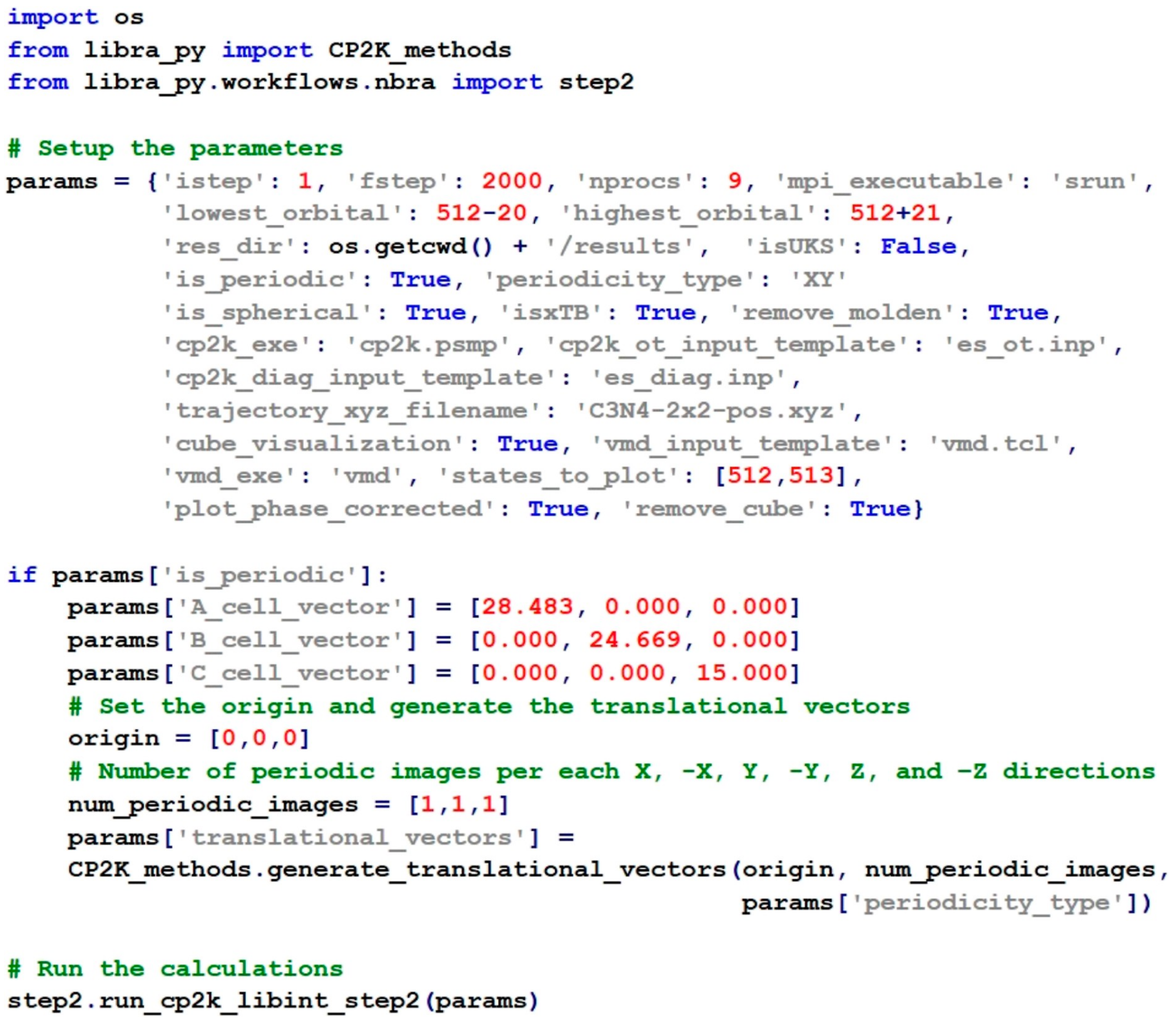

```
import os
from libra_py import CP2K_methods
from libra_py.workflows.nbra import step2

# Setup the parameters
params = {'istep': 1, 'fstep': 2000, 'nprocs': 9, 'mpi_executable': 'srun',
          'lowest_orbital': 512-20, 'highest_orbital': 512+21,
          'res_dir': os.getcwd() + '/results',  'isUKS': False,
          'is_periodic': True, 'periodicity_type': 'XY'
          'is_spherical': True, 'isxTB': True, 'remove_molden': True,
          'cp2k_exe': 'cp2k.psmp', 'cp2k_ot_input_template': 'es_ot.inp',
          'cp2k_diag_input_template': 'es_diag.inp',
          'trajectory_xyz_filename': 'C3N4-2x2-pos.xyz',
          'cube_visualization': True, 'vmd_input_template': 'vmd.tcl',
          'vmd_exe': 'vmd', 'states_to_plot': [512,513],
          'plot_phase_corrected': True, 'remove_cube': True}

if params['is_periodic']:
    params['A_cell_vector'] = [28.483, 0.000, 0.000]
    params['B_cell_vector'] = [0.000, 24.669, 0.000]
    params['C_cell_vector'] = [0.000, 0.000, 15.000]
    # Set the origin and generate the translational vectors
    origin = [0,0,0]
    # Number of periodic images per each X, -X, Y, -Y, Z, and -Z directions
    num_periodic_images = [1,1,1]
    params['translational_vectors'] =
    CP2K_methods.generate_translational_vectors(origin, num_periodic_images,
                                                params['periodicity_type'])

# Run the calculations
step2.run_cp2k_libint_step2(params)
```

Figure 2. Example snippet to run the MO overlap calculations for a 2 × 2 C_3N_4 monolayer.

very first nuclear step in each MD job, we use this technique. Specifically, the converged wavefunction at time *t* is used as the guess wavefunction for the SCF calculations in step *t* + Δ*t*. This approach enables accelerating the calculations significantly. For example, the electronic structure calculations is sped up by about 2.3 times for the largest Si NC using this technique.

It is known that direct diagonalization techniques used in solving the SCF problem may be difficult or even impossible to converge, especially for large systems.[76] Indeed, during our experiments using the implemented xTB method in CP2K, we found some instability in the SCF convergence of some structures using the diagonalization method, namely, when we considered inorganic systems such as titanium-based MIL-125-NH_2 MOF. This problem is due to the short-range part of the anisotropic electrostatic potential and multipole expansion of energy in xTB as has been discussed in detail by Bannwarth et al.[73] On the contrary, the orbital transformation (OT) methodology uses a direct minimization of the energy functional by optimizing the orbitals. This technique proved to be much more robust in our calculations, as expected. However, the OT method only optimizes the occupied orbitals and does not include the unoccupied orbitals. Thus, we developed a hybrid approach. First, an OT-based calculation is conducted to optimize the occupied orbitals. Second, the computed orbitals are used as the initial guess in the diagonalization-based method. The desired number of unoccupied orbitals is considered in the second (diagonalization-based) step. Thus, at the user level, one needs to provide two templates for the desired calculations, one for the OT-based calculations and another for the diagonalization-based step. With this technique, we are able to perform electronic structure calculations for non-metallic inorganic structures using xTB in CP2K. We refer the reader to other references for detailed information on the OT and direct diagonalization methodologies as they are implemented in CP2K.[75,76]

The Libint library is also used by the nano-qmflows package[17,135] for computing the MO overlaps, which is interfaced with CP2K. Both Libra and nano-qmflows can efficiently compute the MO time−overlaps for a large number of states. Beside some programming details, the key difference among the two packages is that although nano-qmflows uses Libint, the computation of the time−overlap matrix in xTB is not yet implemented. In addition, the present implementation extends the calculations to the case of periodic systems. At the moment, only the case of single k-point states is available.

Considering the scale of the systems in this work, we faced another problem. Namely, the size of the numerous coupling or time−overlap files produced along the MD trajectories (each containing N^2 entries, with N being the number of the dynamical basis functions) can easily reach dozens if not hundreds of gigabytes. At the same time, many entries in such files are negligible. For efficient storage of large time−overlap or NAC matrices on the disk, we use sparse binary format, realized in the scipy.sparse library. Finally, our implementation is made to be as user-friendly as possible. Figure 2 illustrates a snippet of the Libra input script for computing the MO overlap and time−overlap matrices for a MD trajectory of a graphitic carbon nitride sheet in xTB. The option to visualize the evolution of frontier KS orbitals by producing and plotting the corresponding "cube" files is also enabled. Samples of such animation of the adiabatic evolution of KS orbitals are included in the Supporting Information for this work. As an example, we also provide the evolution of both phase-corrected[132] and phase-uncorrected frontier KS's for both types of systems. The visualization is done using VMD software[136] and the "tcl" scripts developed in this work are available online.[137]

The main function to call is "run_cp2k_libint_step2" function of the "libra_py.workflows.nbra.step2" module. The time−overlaps computed using this approach are in good agreement with the grid-based approach using the "cube" files we reported earlier[29,30,85] (see Section S2 in the Supporting Information for the comparison of the computations). Other parameters are descriptive but detailed information about all the variables along with different examples for xTB and DFT calculations are available in the Libra code GitHub repository.

2.4. Computational Details: Electronic Structure Calculations. In the electronic structure calculations of Si NCs, the systems are centered in the simulation box by adding about 7 Å of vacuum to each side. The AO basis set for each atom is described by a minimal valence basis with spherical Gaussian-type orbital functions that approximates a Slater-type orbital.[72] These basis sets are optimized and available in CP2K for all elements from H to Rn. The number of unoccupied orbitals included in the electronic structure calculations for each geometry is at least 20% of the number of occupied states for better convergence. The number of considered unoccupied orbitals is chosen to support the single-particle-level excitation of at least 1.0 eV above the lowest unoccupied orbital (LUMO) in NA-MD, to model experimentally studied processes of hot carrier relaxation.[138−140] SCF iterations are continued until the charge density is converged below 10^{-6} Bohr^{-3}. In DFT calculations, a double zeta-valence-polarized basis set is used for the valence electrons of Si and H atoms.[141] A charge density cutoff of 300 Ry is used to select the plane-wave basis that is used to better represent the charge density. The effect of the core electrons is accounted via the Goedecker−Teter−Hutter pseudopotentials.[142−144] Exchange and correlation of valence electrons (in DFT calculations) is accounted for by the Perdew−Burke−Ernzerhof (PBE) exchange−correlation functional[145] augmented with Grimme's DFT-D3 dispersion correction.[146] All the electronic structure properties are calculated in the K-point (0,0,0), the Γ point.

For geometry optimization, the Broyden−Fletcher−Goldfarb−Shannon algorithm[147] is adopted with a maximum force of 15 meV/Å and a maximum displacement of 0.002 Bohr between each 2 geometry optimization steps. The MD trajectories are computed starting with the optimized structures with momenta selected from the Maxwell−Boltzmann distribution for temperature T = 300 K. The MD calculations are conducted within the canonical ensemble, using canonical sampling through a velocity rescaling thermostat[148] with a 15 fs time constant, corresponding to frequencies of the Si−H stretch mode at 2200 cm^{-1}.[149−151] A total of 3 ps MD trajectory is obtained for each NC with a time step of 0.5 fs due to the presence of hydrogen atoms in the Si NC systems. Furthermore, we generate MD trajectories with 0.25 fs time step for 6000 steps to validate the convergence of the NACs computed for the MD trajectory with 0.5 fs time step. We use the same MD protocol for the C_3N_4 and MIL-125-NH_2 MOF structures, except that the time step is increased to 1 fs. Out of a total of 3000 time steps for each trajectory, the first 1000 steps are disregarded as a thermalization period. The last 2000 steps of the MD trajectory are used to compute the time−overlap matrices and NACs for all systems and structures.

2.5. Computational Details: NA-MD Calculations and Their Analysis. For each Si NC, 1 ps (based on 2000 MD production steps with the 0.5 fs integration time step) of NA-MD simulation is computed, considering all states with energies of about 1.0 eV above the first excited state. Four initial excited states with energies corresponding to the desired initial excitation energy level are chosen. Each set of simulations is repeated 6 times (in six parallel batches), thus counting toward 24 simulations for each system. Each simulation utilizes 100 stochastic realizations of the selected TSH/decoherence algorithm. The role of decoherence is assessed by conducting simulations using the decoherence schemes such as the mSDM[115,152] and the ID-A.[114] The hot-electron relaxation dynamics for all NCs are performed in the SAC basis.

Then, the excess excitation energy is computed as the weighted average of the energy levels occupied by all trajectories

$$E(t) = \sum_i \Delta E_i(t) p_i(t) \tag{29}$$

Here, $p_i(t) = N_i(t)/N$ is a fraction of trajectories in state i at any given time t, $N_i(t)$ as computed by the TSH algorithms, N = 100 is the total number of TSH stochastic realizations in each batch, and ΔE_i is the energy of state i relative to the lowest excited-state energy, S_1, of that state at each time moment. Note that the energy for each single-particle excitation is defined as the ground-state energy plus the occupied and unoccupied orbital energy gap. The kinetics of the excess excitation energy decay is approximated by a Gaussian-exponential function of the following form

$$f(t, E_0) = A \exp\left(-\left(\frac{t}{\tau_1}\right)\right) + (E_0 - A) \exp\left(-\left(\frac{t}{\tau_2}\right)^2\right) \tag{30}$$

and the overall timescales are then computed using:

$$\tau = \frac{A}{E_0}\tau_1 + \frac{(E_0 - A)}{E_0}\tau_2 \tag{31}$$

The probability distribution function, $f(x_i)$, of the NAC values, $\hbar|d_{ij}|$, is obtained from computing the derivative of the cumulative distribution function, $F(x_i)$, which is obtained for an interval of $[0,x_i]$ as

$$F(x_i) = \sum_{0 \le x \le x_i} f(x) \tag{32}$$

Then, the probability distribution function for the interval of $[x_{i-1}, x_i]$ is computed as

$$f(x_i) = \frac{F(x_i) - F(x_{i-1})}{x_i - x_{i-1}} \tag{33}$$

Here, we compute the probability distribution function of NAC values for intervals of 0.1 meV.

For NA-MD simulation of the electron−hole recombination in the C_3N_4 monolayer and MIL-125-NH_2 MOF systems, we perform the dynamics using FSSH with and without decoherence schemes such as the DISH[117] and ID-A[114] methods and average over 500 initial geometries with N = 1000 stochastic surface hopping trajectories. We performed the electron−hole recombination dynamics in both SAC and non-SAC bases. For each system, we consider a different number of states involved in the dynamics. For the C_3N_4 monolayer, we consider only two states in the dynamics, the ground state and the first excited state. For the MIL-125-NH_2 MOF, we involve up to 3 excited states to compare with previous DFT-based NA-MD studies of electron−hole recombination in this system. For both systems, the dynamics is also performed by involving more nonradiative channels, up to 0.25 eV above the first excited state, which are selected from all of the excitation energies from the first 5 occupied orbitals to the first 5 unoccupied orbitals near the band edges, which counts to 25 states for the graphitic C_3N_4 monolayer and 13 states for the MIL-125-NH_2 MOF.

The kinetics of the excitation energy decay is best described by the exponential function

$$f(t) = \exp\left(-\frac{t}{\tau}\right) \tag{34}$$

The error bars for the fitted τ values are computed for a confidence interval of 95% using the following statistical formula

$$\varepsilon = Z\frac{\sigma}{\sqrt{n}} \tag{35}$$

Here, the Z value for the selected confidence interval is 1.96, σ is the standard deviation of the data (timescales) and n is the number of fitted data points (simulations) with a R^2 value of higher than 0.9 and 0.1 for hot-electron relaxation in Si NCs and electron−hole recombination in 2D graphitic carbon nitride and MIL-125-NH_2 MOF, respectively.

3. RESULTS AND DISCUSSION

We demonstrate the capabilities of the developed xTB/NA-MD workflow by modeling (a) hot-electron relaxation dynamics in finite Si NCs with diameters extending to as large as 3.5 nm, and (b) electron−hole recombination dynamics in a periodic graphitic carbon nitride monolayer and a titanium-based MOF system. Specifically, we consider the following Si NC structures: $Si_{59}H_{60}$ (1.2 nm), $Si_{123}H_{100}$ (1.6 nm), $Si_{265}H_{140}$ (2.4 nm), $Si_{329}H_{172}$ (2.5 nm), $Si_{501}H_{228}$ (2.8 nm), and $Si_{1009}H_{412}$ (3.5 nm).[153] We also consider a 2 × 2 supercell of graphitic carbon nitride (C_3N_4), containing 96 carbon and 128 nitrogen atoms and the MIL-125-NH_2 MOF unit cell, containing an overall of 264 atoms. Furthermore, for Si NCs, we compute the NACs at the DFT level of theory for all NCs for 1000 geometries (500 fs) of the xTB MD trajectory. Also, we compute the NACs for 2000 steps (500 fs) of the MD trajectory with a smaller time step of 0.25 fs, using the xTB framework, to check the convergence of the NACs with the 0.5 fs time step. For C_3N_4 and MIL-125-NH_2 MOF systems, the NACs are computed only at the xTB level of theory.

3.1. Silicon Nanoclusters.

As a first illustration of the developed methodology, we consider the modeling of hot carrier relaxation dynamics in a series of Si NCs ranging from 1.2 nm ($Si_{59}H_{60}$) to 3.5 nm ($Si_{1009}H_{412}$) in diameter (Figure 3), approaching the size of experimentally studied Si NCs.[154]

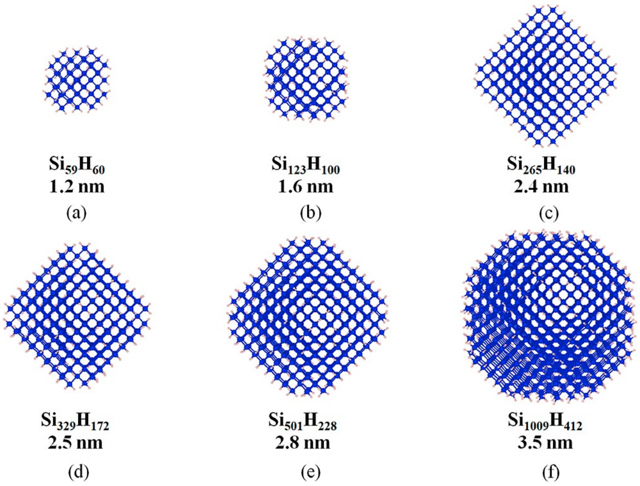

Figure 3. Molecular structures of Si NCs: (a) $Si_{59}H_{60}$; (b) $Si_{123}H_{100}$; (c) $Si_{265}H_{140}$; (d) $Si_{329}H_{172}$; (e) $Si_{501}H_{228}$; and (f) $Si_{1009}H_{412}$.

Earlier, the Kanai group[38] had studied hot-electron relaxation dynamics in Si NCs up to 1.5 nm in diameter. They utilized an approach similar to the present one, although formulated in terms of more expensive DFT-derived KS orbitals. Using a NAC-free DFTB-based approach rooted in the Belyaev−Lebedev[63] formulation of Landau−Zener theory, Smith and Akimov[28] considered Si NCs with a diameter up to 2.2 nm. The use of the xTB approach in the current work allows us to overcome these limits and to model Si NCs as large as 3.5 nm in diameter. To the best of our knowledge, the latter system constitutes the largest Si NC for which the NA-MD simulations have been conducted so far.

The projected density of states (pDOS) of the Si NCs averaged over 2 ps of MD trajectory suggests the localization of the frontier valence and conduction band orbitals on the Si atoms (Figure 4). These MOs are composed primarily of Si 3p and Si 3d orbitals respectively. The hydrogen atom contribution to the DOS is negligible at these energy levels. As expected, the DOS increases with the NCs' diameter. As an implication for the NA-MD computations, one needs to include a larger number of unoccupied orbitals in larger Si NCs to span the same window of excitation energies of interest.

Following the expectations from the quantum confinement considerations, the band gap decreases as the diameter of Si NC increases. Although the observed trends for the computed band gaps do agree with the existing experimental and computational data, the computed band gaps are systematically underestimated compared to the reference values (Table 1). The discrepancy between the xTB and reference band gaps is rather low for large systems (e.g., 1.37 xTB vs 1.59 eV exp. for the 3.5 nm NC), but increases for smaller systems (e.g., 1.9 xTB vs about 3.0 eV exp. for the 1.2 nm NC). We attribute this trend to the use of the single-particle description of excitations

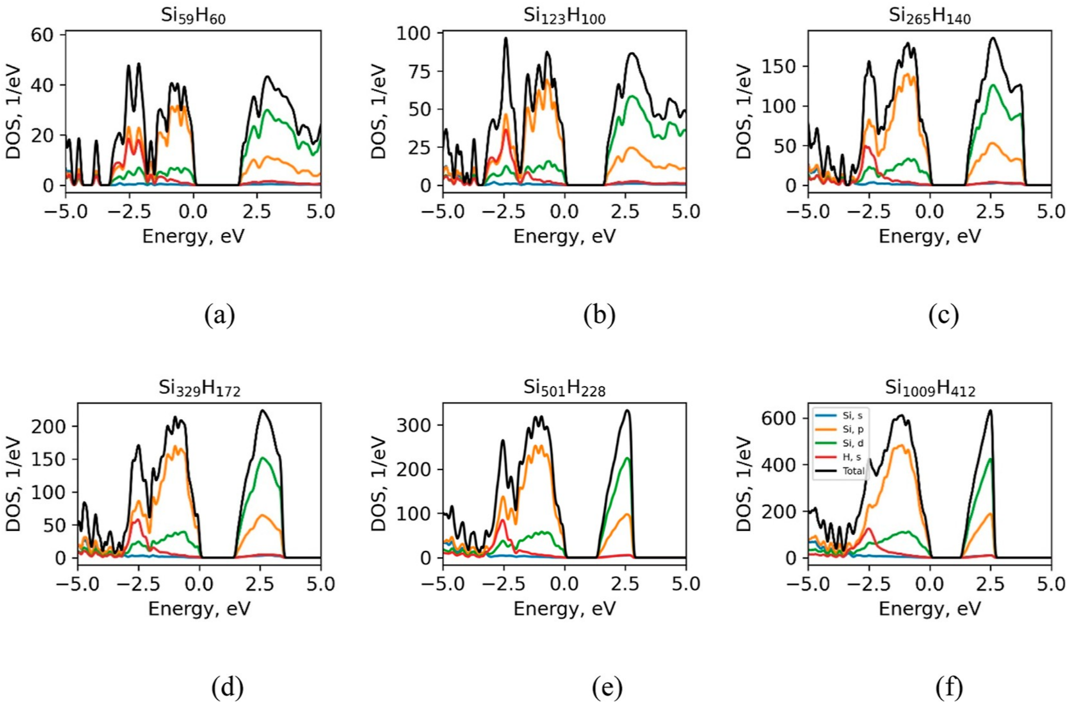

Figure 4. Average pDOS over 2 ps of MD trajectory at 300 K for (a) $Si_{59}H_{60}$, (b) $Si_{123}H_{100}$, (c) $Si_{265}H_{140}$, (d) $Si_{329}H_{172}$, (e) $Si_{501}H_{228}$, and (f) $Si_{1009}H_{412}$. The Fermi energy level is set to zero.

Table 1. Average Band Gaps of the Si NCs Computed in xTB and DFT Frameworks

	computed average band gap, eV		
system and diameter (nm)	xTB	DFT (PBE)	reference band gap, eV
$Si_{59}H_{60}$ (1.2)	1.91	2.58	3.0 (exp)[155]
$Si_{123}H_{100}$ (1.6)	1.73	2.09	2.01 (PBE),[156] 3.09 (HSE06)[156]
$Si_{265}H_{140}$ (2.4)	1.55	1.72	2.08 (exp),[157] 2.3 (exp)[155]
2−3			2.25−2.75 (exp)[139]
$Si_{329}H_{172}$ (2.5)	1.54	1.58	1.9 (exp)[155]
$Si_{501}H_{228}$ (2.8)	1.42	1.36	1.44 (PBE),[156] 2.34 (HSE06)[156]
$Si_{1009}H_{412}$ (3.5)	1.37	1.20	1.59 (exp),[138] 1.19 (PBE),[156] 2.18 (HSE06)[156]
4.0			1.48 (exp),[140] 1.76 (exp)[157]

in the Si NCs in this work as well as to the approximate treatment of electronic exchange and correlation within the xTB method. For small NCs, the confinement effects become significant, and so it is critical to capture the many-body interactions and accurately represent electronic correlations in these systems to yield electronic transition energies in a better agreement with experimental values. For larger systems, the excitonic effects are of a lower importance, so the xTB band gaps are in a better agreement with the reference experimental data. At the same time, the xTB band gaps reasonably agree with the corresponding DFT counterparts. The trends are similar: the discrepancy between the xTB and PBE gaps is higher for smaller Si NCs (e.g., 1.9 eV xTB vs 2.6 PBE eV for d = 1.2 nm NC) but becomes smaller for larger systems (e.g., 1.37 xTB vs 1.2 PBE eV for d = 3.5 nm NC). The discrepancy between the xTB and PBE band gaps can be attributed to the approximations within xTB itself (e.g., the Taylor expansion of the functional) as well as to different bases (tight-binding vs AOs/PWs) used within each method. Nonetheless, the difference between the xTB and PBE band gaps is much smaller than the difference between xTB and experimental reference values, especially in smaller systems. This observation suggests that xTB is still a reasonable approximation to the PBE for these classes of systems and for the problem of interest (the approximate modeling of excited states).

Furthermore, a careful comparison of energies of the utilized dynamical basis states (chosen as the SDs with excitations of the HOMO → LUMO + n kind) and the energy gap distributions computed using xTB and DFT shows that the xTB approach agrees with the DFT quite closely (Figures S1 and S2). The PBE method yields somewhat larger gaps between the adjacent states than the xTB, especially for smaller systems. However, such differences are rather small and vanish as the system's size increases. The slight discrepancy of the xTB and DFT energy gaps can be attributed to the difference in treatment of the long-range exchange interactions. Although the PBE functional used in the current DFT calculations has a relatively short-ranged exchange potential (as all pure functionals typically do), it is longer ranged than the truncated xTB expression, leading to somewhat smaller adjacent-state energy gaps in the xTB calculations compared to the PBE counterparts. The PBE values are also not ideal, due to the incorrect long-range asymptotic behavior of pure exchange functionals. This is also manifested in the discrepancies between the computed PBE band gaps and the experimental or HSE values (Table 1). These variations of the energy gaps are likely to affect the NAC magnitudes and the electron relaxation rates. Specifically, we expect that xTB NACs and NA relaxation rates may be somewhat overestimated in comparison to the real values. Indeed, as our calculations show (vide infra), the computed hot carrier relaxation rates are several times smaller than the corresponding experimental values.

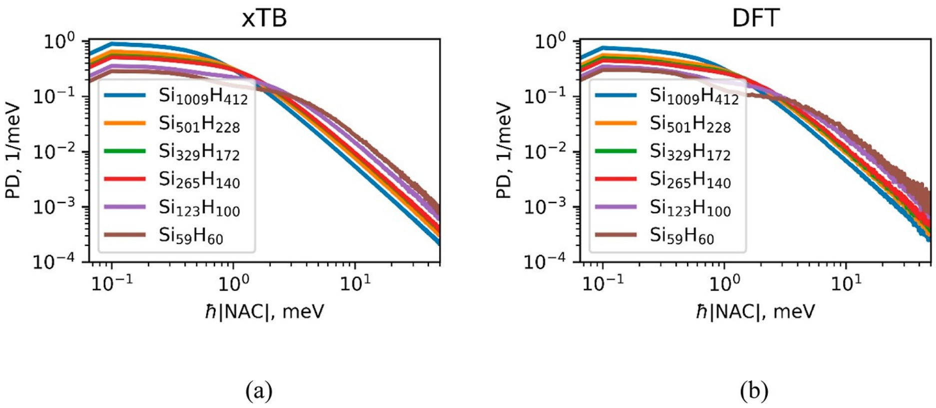

(a) (b)

Figure 5. Probability distribution of NAC magnitudes between all pairs of electron-only excitation basis within an energy window of 1.0 eV above the first excited state for all Si NCs computed with: (a) xTB and (b) DFT methods.

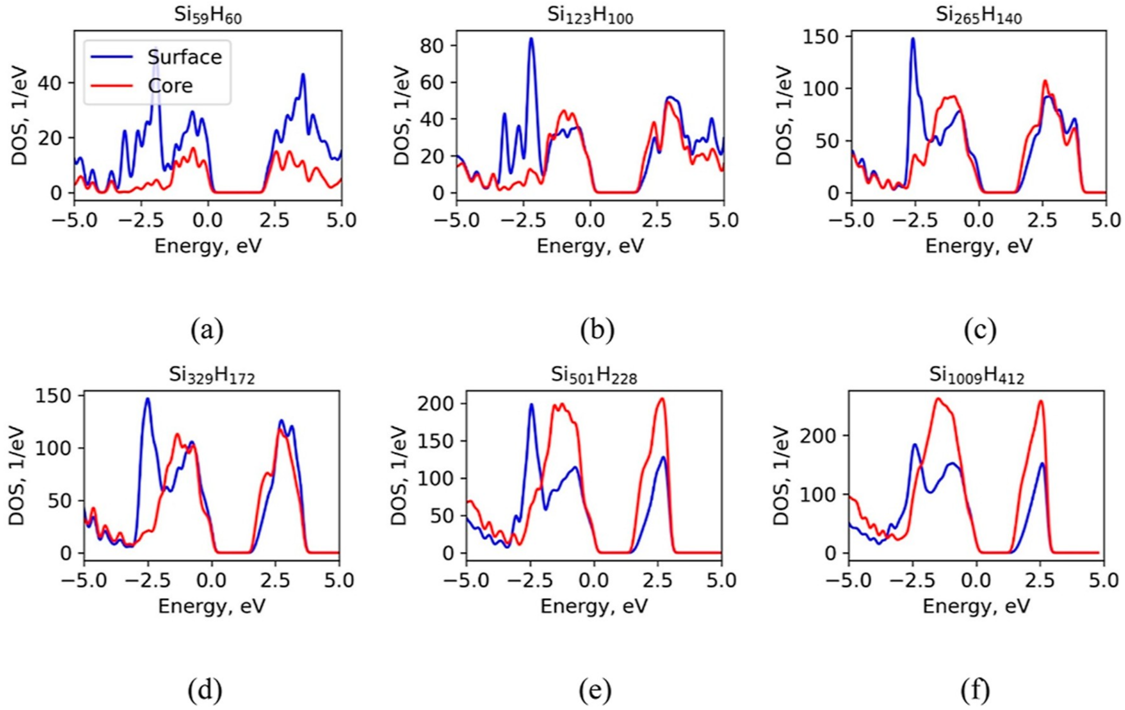

(a) (b) (c)

(d) (e) (f)

Figure 6. Core/surface-resolved pDOS of the optimized geometries for (a) $Si_{59}H_{60}$, (b) $Si_{123}H_{100}$, (c) $Si_{265}H_{140}$, (d) $Si_{329}H_{172}$, (e) $Si_{501}H_{228}$, and (f) $Si_{1009}H_{412}$. The Fermi energy level is set to zero.

The largest Si NC considered in this work involves 2724 single-particle states making the DFT-based calculations much more time-consuming than the xTB-based calculations. For example, the average timing of an SCF cycle to complete, including both OT and diagonalization together, is about 3.5 times faster for xTB than for DFT for the largest Si NC. Consistent with the increased DOS for larger NCs, the mean of the probability distribution for energy gaps between adjacent states shifts toward smaller values as the system size increases but is converged rapidly with the system's size (Figure S2). This rapid convergence and the weak sensitivity to system's size are likely due to the lack of proper long-range behavior of the xTB exchange−correlation functional. Indeed, the short-range behavior of the xTB functional has been mentioned in the original formulation[72,73] and was also related to potential convergence problems in systems with nearly degenerate states.

We compute the probability distribution of the magnitudes of NACs between all pairs of states, $\hbar|d_{i,j}|$, for all systems using orbitals obtained from PBE and xTB calculations (Figures 5 and S3). The statistics is based on 4000 data points (2 ps trajectory, 0.5 fs time step) for xTB and 1000 data points (500 fs trajectory, 0.5 fs time step) for DFT. It is known that the numerical calculations of NACs can be dependent on the selected nuclear time step.[158,159] To check the appropriateness of the chosen timestep, we also compute NAC distributions with a smaller time step of 0.25 fs using 2000 data points (a 500 fs trajectory). Our calculations (Figure S4) suggest that NAC calculations are converged using a 0.5 fs time step already.

Our intuitive expectation is that NAC should increase on average with increasing the NC diameter because the average energy gap between the adjacent states would decrease. However, we observe a nearly opposite situation—first, there is a higher probability to observe smaller NAC magnitudes (e.g. below 1−2 meV) in larger NCs (Figures 5 and S3, panels a and d). Second, as one moves to larger NACs, above 2 meV, there is a clear trend to more likely observe larger NACs in smaller NCs (Figures 5 and S3, panels b, c, e, and f). To explain such an unusual result, we recall that there are two major factors that can affect NAC magnitudes: (1) the electronic structure method itself (e.g., DOS and state localization) and (2) the details of nuclear dynamics, such as the magnitude of average fluctuation of the nuclear DOFs that couple the electronic states of interest. The analysis of the projected densities of states indicates that the core states (as opposed to surface states) become dominant in the composition of the frontier (and nearby) states when the NC size increases (Figure 6). At the same time, the core Si atoms experience smaller coordinate fluctuations (Table 2) and therefore exert a smaller perturbation on the NC-core electronic states. As a result, the NAC which quantifies the response of electronic states on the perturbation of nuclear geometry decrease in larger NCs. Furthermore, the spatial separation of orbitals increases as the diameter of NCs increases (Figures S5 and S6). Indeed, in small NCs, the orbitals may be delocalized over the entire NC. Thus, the time−overlaps of different orbitals may be notable. In contrast, in large NCs, the orbitals are localized only within a finite region of the NC. Thus, the distinct orbitals may be notably separated in space, leading to smaller time−overlaps. Recall that the regular, that is, same-time, overlaps of distinct orbitals are still zero due to their orthogonality, no matter their spatial localization. However, the orthogonality condition does not hold for the time−overlaps, in which case the spatial localization of orbitals is important.

Table 2. Root Mean Square Deviation of Atomic Positions of Core and Surface Si Atoms, Angstrom

system	Si-surface	Si-core
$Si_{59}H_{60}$	0.273	0.172
$Si_{123}H_{100}$	0.152	0.113
$Si_{265}H_{140}$	0.144	0.114
$Si_{329}H_{172}$	0.186	0.141
$Si_{501}H_{228}$	0.262	0.190
$Si_{1009}H_{412}$	0.169	0.127

We also compute the average pure dephasing times in all Si NCs for all pairs of states within a 1.0 eV excitation energy window (Figure S7). We observe that these times increase with the increase of the NC diameter and can be as large as several hundred femtoseconds. The observed dependence can be rationalized by the increased DOS in larger Si NCs, which leads to smaller energy gaps, and hence to smaller energy gap fluctuations. Indeed, as Figure S1 illustrates the energy levels of Si NCs constitute a very dense band with nearly parallel energy levels. As a consequence of large dephasing times, one can expect the significance of coherent dynamics in such systems.

Finally, we conduct TSH calculations for all six systems, using the FSSH, ID-A, and mSDM methods. A representative evolution of the excess excitation energy for the smallest and the largest systems considered is shown in Figure 7 with all the cases shown in Figure S8. The computed timescales are summarized in Table 3.

The FSSH calculations suggest that hot carriers with an initial excess excitation energy of 1.0 eV relax within 102−133

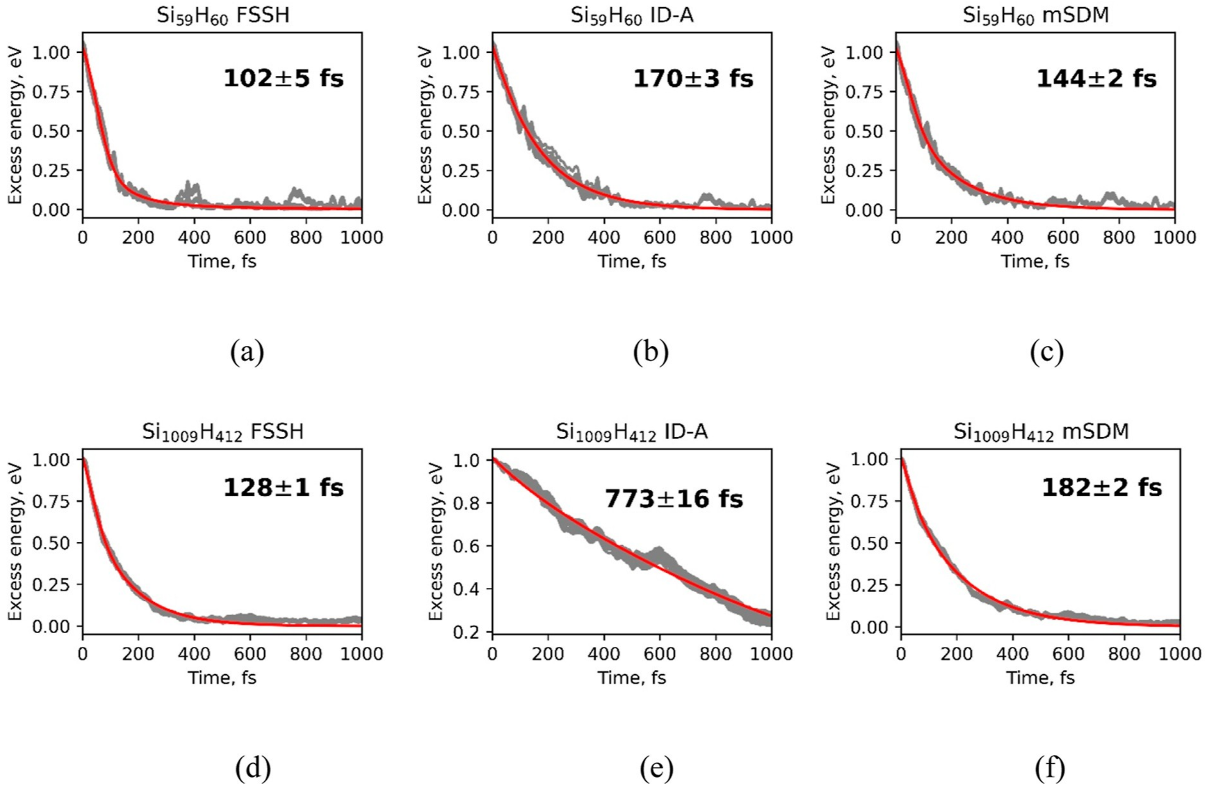

(a) (b) (c)

(d) (e) (f)

Figure 7. Representative dynamics of hot electron excess excitation energy relaxation in Si NCs with initial 1.0 eV excitation above LUMO using: (a,d) FSSH, (b,e) ID-A, and (c,f) mSDM for (a−c) $Si_{59}H_{60}$ and (d−f) $Si_{1009}H_{412}$ systems. Solid red lines correspond to the average fitting with the Gaussian-exponential function.

Table 3. Hot Electron Relaxation Timescales Obtained from Fitting the NA-MD Results to a Gaussian-Exponential Function in Eq 28

	relaxation time			
system/size	FSSH	ID-A	mSDM	reference data, fs
$Si_{59}H_{60}$ (d = 1.2 nm)	102 ± 5	170 ± 3	144 ± 2	1.5 nm 1.0 eV, 400 fs (comp),[38] 182 fs (comp)[28]
$Si_{123}H_{100}$ (d = 1.6 nm)	109 ± 1	286 ± 3	173 ± 3	
$Si_{265}H_{140}$ (d = 2.4 nm)	114 ± 1	455 ± 7	177 ± 2	2.2 nm 1.0 eV, 59 fs (comp)[28]
$Si_{329}H_{172}$ (d = 2.5 nm)	133 ± 3	494 ± 7	192 ± 3	
$Si_{501}H_{228}$ (d = 2.8 nm)	131 ± 1	617 ± 12	197 ± 1	~2−3 nm, ~0.45−0.9 eV, ~600 fs[139] (exp)
$Si_{1009}H_{412}$ (3.5 nm)	128 ± 1	773 ± 16	182 ± 2	3.5 nm, 0.44 eV, 720 fs (exp),[138] 4.0 nm, 1.0 eV, 380 fs (exp)[140]

fs. These values are a factor of 4−5 smaller than the timescales reported in the experiment or suggested by other computations but larger than the timescales obtained by the BL-LZ dynamics[28] (Table 3). The mSDM calculations suggest a 1.5× slower relaxation reducing the discrepancy with the experiment to a factor of 2−3. Importantly, the relaxation times computed with either the FSSH or mSDM methods show a non-monotonic dependence on the NC diameter. These times increase as the diameter of the Si NC increases up to 2.5−2.8 nm. After this critical size, the relaxation times start decreasing as the Si NC diameter continues to increase. This trend is consistent qualitatively with the experimental results of Bergren et al.[138] who reported a similar non-monotonic dependence of the excess excitation energy cooling times in Si NCs. In their work, four Si NCs with average sizes of 3.4, 4.7, 6.2, and 7.3 nm were considered. The slowest hot carrier relaxation was found for the 4.7 nm NC. However, it was found to accelerate again as the NC diameter increases to 6.2 and 7.3 nm.

The non-monotonic dependence of excitation energy relaxation times on the Si NC diameter can be rationalized in the following way. The excess energy relaxation depends on the NAC magnitudes that determine the rates of population transfer, as well as on the DOS, which determines the likelihood of the "parallel", across-the-state transitions or kind transitions $\Psi_{\text{HOMO}}^{\text{LUMO}+i} \rightarrow \Psi_{\text{HOMO}}^{\text{LUMO}+j}$ with $|i - j| > 1$. As illustrated in Figure 5, the probability to encounter larger NACs is higher for smaller NCs. These large NACs would be the dominant factor that leads to a fast energy relaxation in smaller Si NCs. As one moves to larger systems, the probability density to sample configurations with smaller NACs increases, and the small-NAC transitions become dominant; the computed lifetimes increase. As one goes to even larger NCs, the number of possible non-adjacent state transitions within a given energy window increases, and the energy relaxation rates increase due to the dominance of the increased number of relaxation channels. The number of indirect transitions of such kind increases roughly quadratically with the density of electronic states. The transitions $i \rightarrow i + 2$, $i \rightarrow i + 3$, and so forth have NACs comparable to the NACs of the adjacent transitions, $i \rightarrow i + 1$. The quadratically increasing number of "parallel" channels for energy decay eventually leads to the acceleration of the relaxation dynamics in larger systems.

To support the "parallel"-transfer mechanism and its role in defining the NC-size dependence of the energy relaxation times, we conduct additional restricted calculations in which we zero out all of the NACs between non-adjacent states (Figure S9). Such modified Hamiltonians allow only the transitions between the adjacent states in all of the Si NCs. The results show that the excess excitation energy decays faster in smaller NCs such as $Si_{59}H_{60}$ (Figure S9, panels a−c). The process slows down in the larger $Si_{123}H_{100}$ system (Figure S9, panels d−f). For even larger systems, we do not observe any steady decay over a simulation time of 1 ps (Figure S9, panels g−r). These observations are consistent with our analysis of the NAC distributions that show a decreased probability of the larger NACs in the larger NCs (Figure 5). Thus, the overall acceleration of the excitation energy relaxation in larger systems observed in the unconstrained simulations (Figures 7 and S9) can indeed be attributed to the increased number of relaxation channels rather than to a potential increase of NAC magnitudes.

It is instructive to discuss the methodological differences next. First, the mSDM results are comparable to the results generated by the FSSH method, but the relaxation times are larger on average. This overall closeness of the mSDM results to the FSSH results can be attributed to relatively large dephasing times (Figure S7), which make the corrections to the coherent amplitudes relatively small. However, this correction is helpful because it improves (not notably) the agreement of the computed results with the reference values, especially for larger systems (Table 3). In addition, the position of the slowest relaxation is shifted toward larger systems (e.g., 2.8 nm Si NC for mSDM vs 2.5 nm Si NC for FSSH), in a better agreement with the results of Bergren et al.[138] (e.g., slowest relaxation in 4.7 nm NC).

The ID-A dynamics predicts a monotonic increase of the relaxation lifetimes for Si NCs with the increase of their diameter. The computed lifetimes are nearly an order of magnitude larger than the corresponding FSSH and mSDM values putting them in a better agreement with the experimental references for the 3.5 and 2.8 nm NCs. This difference with the mSDM value can be attributed to the algorithm for handling decoherence. Within the ID-A formulation, the overall coherent superposition collapses periodically to a given state, roughly to the one with the highest quantum population at the moment of collapse. Because the greatest population transfer occurs due to multiple channels for non-adjacent state transitions, the ID-A collapses effectively remove such parallel pathways by destroying the coherences between the non-adjacent states. As a result, we observe a steady increase of the ID-A energy relaxation times with the Si NC size increase, similar to the trend observed in the constrained simulation (Figure S9). Thus, the ID-A favors the consecutive hopping mechanism. As a result, the larger the number of states to traverse through (as is the case in larger NCs), the longer it takes. Furthermore, frequent "resets" of the coherent dynamics by the ID-A slows down the coherent dynamics as well. On the contrary, within the mSDM formulation, all coherent amplitudes are affected gradually, and no abrupt "resets" of the dynamics occur. Such an algorithm favors a faster overall dynamics as observed in the mSDM calculations.

Despite the numerical closeness of the ID-A relaxation times to the experimental reference values (Table 3), the ID-A has a significant conceptual flaw—it destroys coherences where they

https://doi.org/10.1021/acs.jctc.2c00297

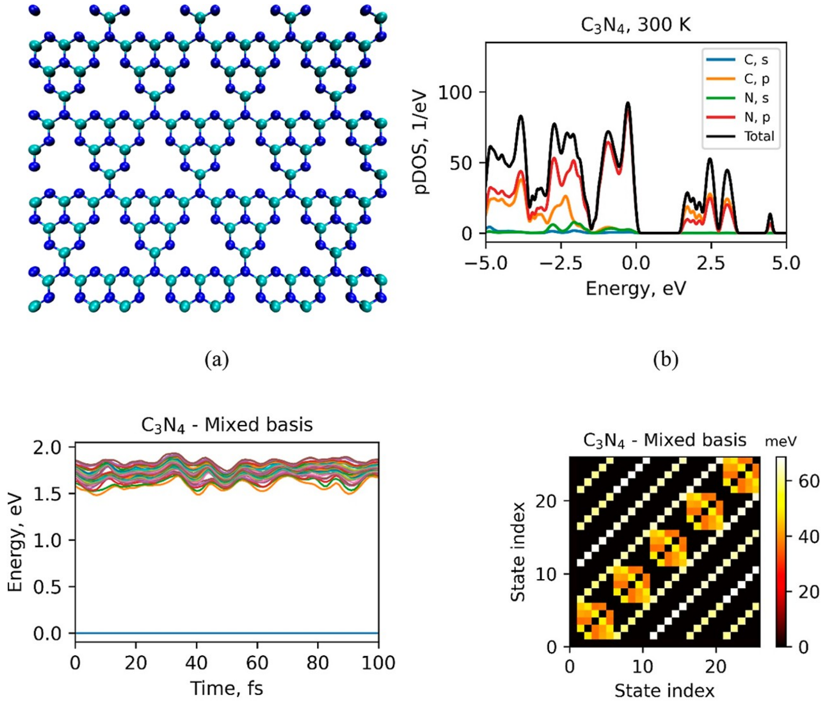

(a) (b)

(c) (d)

Figure 8. Molecular and electronic structure of the graphitic carbon monolayer: (a) molecular structure of a 2 × 2 × 1 supercell of C_3N_4 monolayer; (b) pDOS averaged over 2 ps of MD trajectory at 300 K for the 2D C_3N_4; (c) energies of the mixed electron−hole excited states for a 100 fs sub-trajectory of MD trajectory; and (d) MD-averaged NAC magnitudes for all pairs of the identity-ordered mixed electron−hole excited states.

should be preserved, such as in the systems with dense manifolds of states whose energies evolve nearly parallel to each other (e.g., Figure S1). As a remarkable consequence, the method yields no maximum of the energy relaxation time as a function of NC size. In contrast, the methods that preserve such needed coherences, FSSH and mSDM, are capable of predicting such a turnover in the timescales. Hence, the preservation of coherences by the decoherence algorithms is an important property needed in order to capture such qualitative trends in the timescales.

The reported timescales should be taken with a grain of salt. On the one hand, the present approach relies on the xTB framework, which is optimized to predict the ground-state energetics and geometries, but not necessarily the excited-state properties, as for instance in the ZINDO semiempirical method.[51] As discussed above, the xTB method tends to underestimate energy gaps and may therefore overestimate the NACs (although they are still consistent with the PBE level) and the excitation energy relaxation rates (Table 3). On the other hand, the current approach relies on a single-particle (orbital) treatment of excited states. As we demonstrated recently, true excited states in systems such as Si NCs are multiconfigurational, and the inclusion of such effects leads to an acceleration of the dynamics.[29] Thus, the current quantitative disagreement of the computed timescales with the experimental values may potentially be resolved by incorporating the excitonic effects.

3.2. Graphitic Carbon Nitride Monolayer. As a second illustration of the developed methodology, we consider modeling of electron−hole recombination in a periodic 2D system, graphitic carbon nitride (Figure 8a). The electronic pDOS of a 2 × 2 × 1 monolayer supercell computed with xTB and averaged over 2 ps of MD trajectory is shown in Figure 8b. The frontier valence band states are mostly 2p (N) states, whereas the conduction band states are represented by 2p (N) and 2p (C) states, with the latter being the dominant contributions. The MD-averaged band gap of the system is 1.56 eV. This value is underestimated in comparison to the experimental values ranging from 2.79[160] to 2.89 eV[161] but reasonably close to a corresponding PBE value of 1.92 eV.[161] As we discuss in Section 3.1, the underestimation of the PBE calculations with respect to the experimental value can be attributed to a poor description of the long-range part of the exchange functional—the problem that can be fixed using hybrid functionals, especially those with long-range corrections. Indeed, Agrawal et al.[161] report a band gap of 3.26 eV computed with the HSE functional. Our xTB values are also underestimated in comparison to the PBE gap, due to the tight-binding approximation of the exchange−correlation functional as used in the xTB method. Overall, the underestimation of the band gap is rather notable, and it is expected to lead to an acceleration of the nonradiative dynamics. Thus, the timescales we obtain in this work can be regarded as the lower boundary of the true timescales.

Following the earlier work of Agrawal et al.,[161] who conducted simulations in a similar system, although using a PBE/NA-MD approach within the NBRA, we model the nonradiative electron−hole recombination in this system. Although the initial state is chosen as the first excited state of the HOMO → LUMO type, we include 24 excited states in the dynamical basis, to enable additional pathways for recombination, such as the indirect recombination after initial

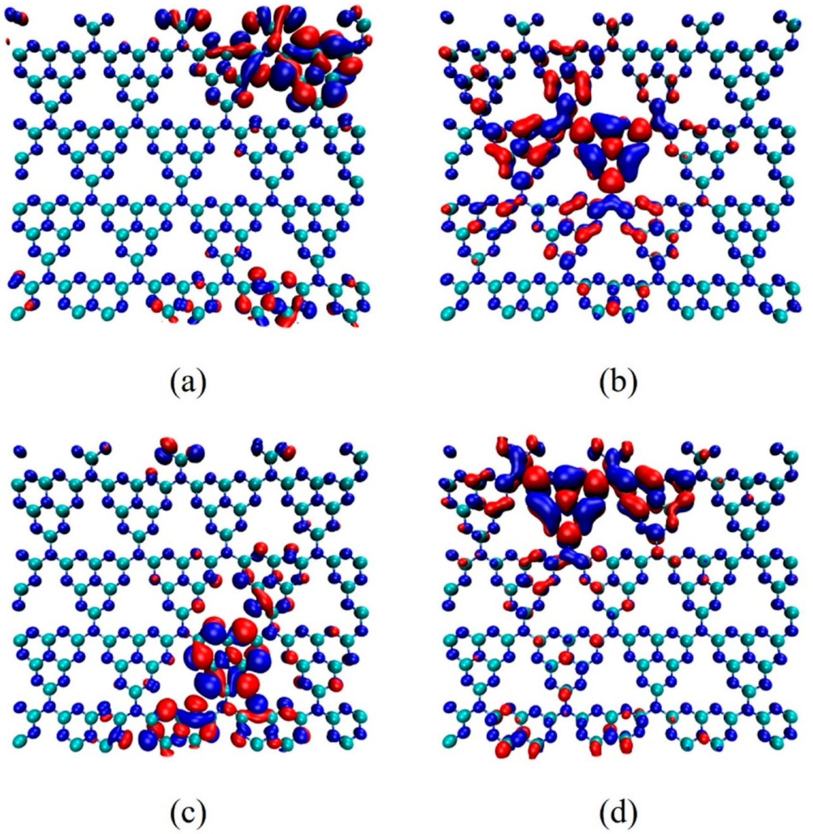

Figure 9. Snapshots of the (a,c) HOMO and (b,d) LUMO isosurfaces (0.01 Bohr^{-3}) of the 2D graphitic carbon nitride at two random MD geometries.

thermal excitation to lower excited states, or the pathways involving the exchange of electron and hole excitation energies. Our basis is composed of HOMO − n → LUMO + m, n = 0, ... 4, and m = 0, ..., 4 excitations. These states span a 0.25 eV window of energies above the S_1 state energy, much larger than the thermal energy quantum at 300 K (Figure 8c). The inclusion of such states in the dynamics enables modeling thermally-activated recombination, in which the initial S_1 state may be promoted to higher-lying states thermally, followed by the direct relaxation of the generated "hot" state to the ground state. We also perform the dynamics by involving only two states (the HOMO → LUMO transition approximating the S_1 state, and the ground state) in the dynamical basis, similar to the setup used previously by Agrawal et al.[161]

Our analysis of the NAC map between the pairs of excited states shows that the most strongly coupled states are adjacent in their indices and correspond to couplings of the type $\langle\Psi^{\text{LUMO}+m}_{\text{HOMO}-n}|\frac{\partial}{\partial t}|\Psi^{\text{LUMO}+m'}_{\text{HOMO}-n}\rangle$ or $\langle\Psi^{\text{LUMO}+m}_{\text{HOMO}-n}|\frac{\partial}{\partial t}|\Psi^{\text{LUMO}+m}_{\text{HOMO}-n'}\rangle$ (Figure 8d). The pairs with both n and m being different, such as $\langle\Psi^{\text{LUMO}+m}_{\text{HOMO}-n}|\frac{\partial}{\partial t}|\Psi^{\text{LUMO}+m'}_{\text{HOMO}-n'}\rangle$ with $n \neq n'$ and $m \neq m'$ are not coupled. The patterned structure of the NAC map in Figure 8d is the consequence of the ordering of the states in the mixed electron−hole excitation basis. Here, the distant-index states could be coupled because they may correspond to excitations with $n = n'$ but $m \neq m'$ or $m = m'$ but $n \neq n'$. At the same time, the next-index points may be decoupled because they may correspond to $n \neq n'$ and $m \neq m'$. The NAC maps can also be computed in the energy-ordered representation (Figure S10a). In this representation, the states of the closest energy normally have the largest coupling. On average, the non-zero coupling will be observed for all pairs of state energies. This is because the energy-ordered states may correspond to different state identities at different times. Thus, the coupling for a given pair of state energies shown in Figure S10a corresponds to the trajectory average of NACs for different pairs of identity-ordered states, both coupled and decoupled originally. Here, we perform the electron−hole recombination dynamics in the energy-ordered basis. Because the physically measured labels of states are their energies, we believe that the energy-ordered basis is the most suitable for modeling the excitation energy relaxation dynamics.

The trajectory-averaged NAC magnitudes for the pair of the S_0 and S_1 states is 0.64 meV, which is nearly 2.8 times smaller than the 1.8 meV value reported by Agrawal et al.[161] This result is counterintuitive to our expectation based on the analysis of the energy gap. In fact, we could expect a factor of $1.92/1.5 \approx 1.3$ increase of the NAC values in comparison to the PBE-based values of Agrawal et al.[161] In contrast, we obtain decreased couplings. One reason for such a discrepancy could be the difference of the computational setups, such as the MD trajectory generation methods, electronic structure method choices, as well as the software implementation used. For instance, the Pyxaid code used by Agrawal et al.[161] does not incorporate the phase-consistency correction to NACs used in the present work. Another reason could be the unit cell size effect. Indeed, the area of the supercell used in the present work is 4 times larger than the area of the unit cell used by Agrawal et al.[161] As a consequence, the orbitals in the computational setup of Agrawal et al. appear delocalized over

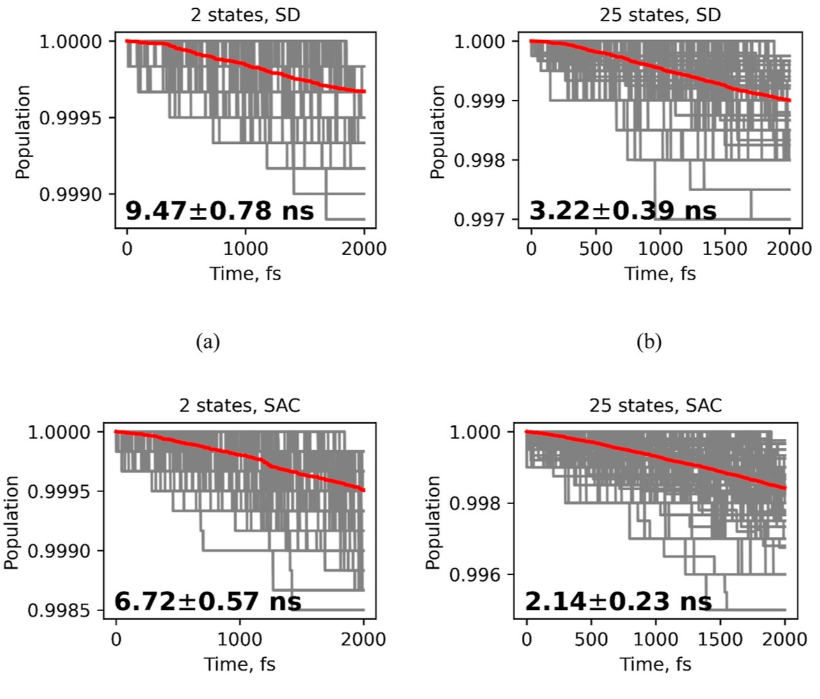

(a) (b)

(c) (d)

Figure 10. Total population of all excited states in the C_3N_4 monolayer as a function of time during a 2 ps NA-MD trajectory. The calculations are conducted using the DISH method with 2 (a,c) or 25 (b,d) states, using the dynamical basis of SD (a,b) or SAC (c,d) states. Gray lines indicate population dynamics of individual matches, while the red line shows the average population.

the entire simulation cell, whereas in our work we observe the localization of orbitals in finite regions of the supercell used (Figure 9 and Supporting Information animations, Videos S4), consistent with the early works of Levine et al.[162] As a consequence, the orbitals are more distant from each other in the present work than they were in the work of Agrawal et al., leading to smaller time−overlaps and NACs.

The excited-state relaxation dynamics, which models the electron−hole recombination is computed using the SD and SAC dynamical bases (Figure 10). In these calculations, the lowest excited state is initially populated, but other excited states may be included in the calculations because they may be transiently populated before the system relaxes to the ground state. In the minimalistic model that used 2 SDs (ground and excited states) in the dynamical basis, we obtain a 9.5 ns timescale (Figure 10a), which is comparable to the 10.8 ns reported previously by Agrawal et al. for the minimal unit cell system and the same dynamical basis.[161] The recombination is 1.4 times faster if the SAC basis is used (Figure 10c). This acceleration factor is comparable to the expected 2× acceleration. Such an acceleration is expected because the effective NAC values between the ground and excited states in the SAC basis are $\sqrt{2}$ times higher than in the corresponding SD basis (e.g., see Section S1 of the Supporting Information). We attribute the deviation of the SAC-acceleration factor from the expected 2 to the quality of the hops sampling within the 1 ps of simulation in very slow processes with an intrinsic timescale of 10 ns. Indeed, repeating the same calculations with the FSSH or ID-A methods yields much faster dynamics (Figure S11), with the expected 2× acceleration clearly reproduced.

We also observe an interesting acceleration of the recombination dynamics when increasing the number of dynamical basis states used in the calculations. For instance, extending it to 25 basis states, the recombination times decrease to 3.2 ns in the SD and 2.1 in the SAC bases (Figure 10, panels b and d). The mechanism of such acceleration is likely similar to the one we observed in the Si NC case. The added states are close in energy to the original state and thus can be easily populated both coherently and in the hopping algorithm. Each of the auxiliary states is likely to develop coherences with the ground state, in parallel. Thus, one can expect a fast coherent population of the ground state. Thus, multiple "parallel" coherent population transfer channels are opened, leading to a faster population transfer between the excited states manifold and the ground state. To verify this hypothetic mechanism, we also compute the relaxation dynamics with the FSSH and ID-A approaches (Figure S11). Similar to DISH, in FSSH calculations, we observe the acceleration of the ground-state recovery in models with more excited states included. This is consistent with our proposed mechanism. Indeed, the FSSH approach allows for the development of multiple coherences and it therefore facilitates opening parallel relaxation channels (similar to Sin NCs case) and it does accelerate the dynamics, as DISH does. On the contrary, in the ID-A calculations, we observe slower dynamics in the model with more excited states. The ID-A algorithm frequently destroys coherences. Adding more states to the system may lead to more frequent hop attempts and hence, more frequent coherence resets. In this case, the additional states act as the "electronic friction bath", whereas in the FSSH or DISH methods, the additional states act as the effective coherence-based facilitators of relaxation. A more detailed investigation of these mechanisms is beyond the scope of this work and will be reported separately.

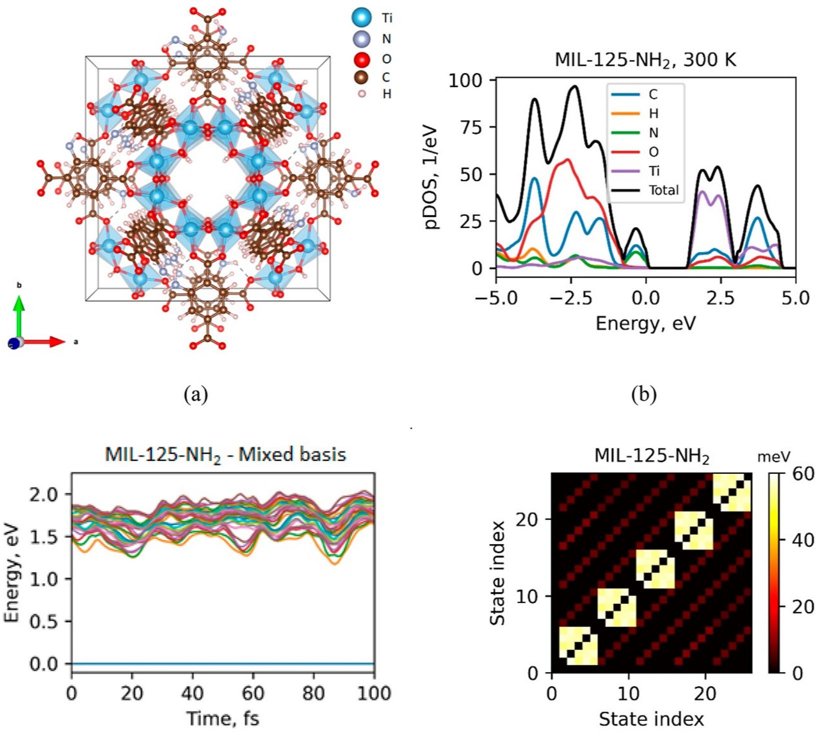

(a) (b)

(c) (d)

Figure 11. Molecular and electronic structure of the MIL-125-NH$_2$ MOF: (a) crystal structure of the titanium-based MIL-125-NH$_2$ MOF supercell; (b) pDOS averaged over 2 ps of MD trajectory at 300 K for the MIL-125-NH$_2$; (c) energies of the mixed electron−hole excited states for a 100 fs sub-trajectory of MD trajectory; and (d) MD-averaged NAC magnitudes for all pairs of the identity-ordered mixed electron−hole excited states.

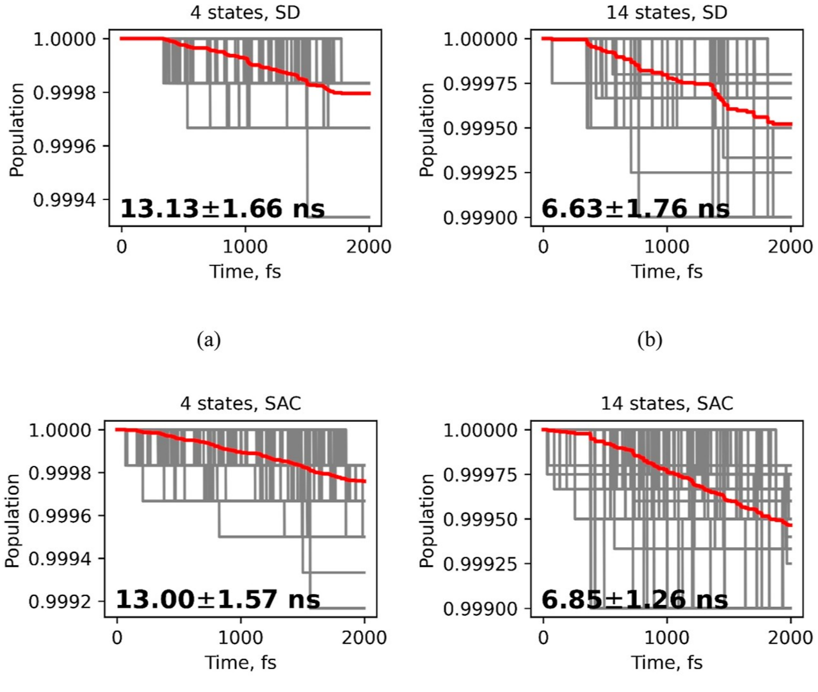

(a) (b)

(c) (d)

Figure 12. Total population of all excited states in MIL-125-NH$_2$ MOF as a function of time during a 2 ps NA-MD. The calculations are conducted using DISH method with 4 (a,c) or 14 (b,d) states, using the dynamical basis of SD (a,b) or SAC (c,d) states. Gray lines indicate population dynamics of individual matches, while the red line shows the average population.

3.3. MIL-125-NH$_2$ MOF. As the third and final example of application of our methodology to modeling NA-MD processes in extended systems, we consider electron−hole recombination dynamics in titanium-based MOF, the MIL-125-NH$_2$ (Figure 11a), previously studied by Syzgantseva and co-workers.[86] The ensemble-averaged pDOS at 300 K shows that the valence band edge states are composed mostly of the C and N atomic states, while the conduction band edge states are mostly composed of the titanium orbitals with a small contribution of C and O atomic states (Figure 11b). An MD-averaged band gap of 1.49 eV computed at the xTB level is only marginally higher than a PBE value of ∼1.35 eV reported by Syzgantseva et al.[86] At the same time the single-particle gaps are about 2.2 times smaller than the ∼3.25 eV experimental gap,[102,163] suggesting that accounting for excitonic effects may be an important next-step refinement of the current single-particle based methodology. Similar to the graphitic C_3N_4 system, we observe that NACs between mixed electron−hole states are the largest for the pairs of energetically adjacent states (Figures 11d and S10b). As expected from the relatively large gap, the NACs between the ground state and other excited states are small, on an order of 0.14 meV. Notably, all excited states near the first one exhibit NACs with the ground state of a comparable magnitude.

Previously, Syzgantseva et al.[86] modeled the dynamics of the ground-state recovery in MIL-125-NH$_2$ MOF using a similar NBRA approach. Considering a minimalistic dynamical basis of the ground and only the first three excited states (of the electron-only excitation type), the electron−hole recombination time of approximately 13 ns was reported. The corresponding NAC of the first excited state (approximated by the HOMO → LUMO transition) to ground state was computed to be 3.09 meV at the PBE level of theory, excluding the $\sqrt{2}$ prefactor that should be included due to SAC.[86] Our xTB-based NAC calculations yield a notably smaller value of ∼0.14 meV (in the SD basis), while the value accounting for spin-adaptation should be larger by a factor of $\sqrt{2}$. A direct comparison of these values is not straightforward because the discrepancies could also be related to the different protocols used to produce MD trajectories, to the differences in the electronic structure calculations themselves, as well as to the differences of the utilized codes. We expect that the differences introduced by the electronic structure calculations to be minimal because both PBE and xTB produce comparable band gaps.

First, we conduct the NA-MD calculations of nonradiative electron−hole recombination in MIL-125-NH$_2$ with the minimalistic four-state basis used by Syzgantseva et al.[86] Unlike in their work, where the three excited states were chosen as the HOMO → LUMO, HOMO → LUMO + 1, and HOMO → LUMO + 2 transitions, we also consider the hole excitation channels, so the three excited configurations used in this work are HOMO → LUMO, HOMO → LUMO + 1, and HOMO − 1 → LUMO. They are the three lowest energy determinants. The system is initially populated in its first excited state and the total population of all excited states is monitored over time (Figure 12, panels a and c). In both the SAC and SD bases, our calculations yield the 13 ns electron−hole recombination time, which is in excellent agreement with the 9−15 ns range reported experimentally by Santaclara et al.[102,164] Despite smaller average NACs and a larger band gap, we obtain a timescale similar to the one reported by Syzgantseva et al.[86] This agreement likely due to other factors such as the difference in the version of the algorithm used, nuclear dynamics, and slightly different dynamical bases used in the two works. In particular, the basis used in this work enables the hole excitations in addition to the electron excitations, whereas the work of Syzgantseva considers only the electron excitation channels.

Similar to the C_3N_4 example, we observe the acceleration of the relaxation dynamics when more than four dynamical basis functions are used. In the model calculations with 13 excited states spanning 0.25 eV above the lowest excited state (Figure 12, panels b and d), we observe a 2-fold acceleration (6.6 ns) of the dynamics in comparison to the one with four-state model. Analogous to the C_3N_4 system, we also observe the acceleration of the dynamics in system with 14 states when using the FSSH method, as well as the deceleration when using the ID-A method (Figure S12). We believe the mechanisms governing these effects are analogous to those discussed in Section 3.2.

Surprisingly, the timescales obtained in the calculations with the SAC basis (13 ns, Figure 12a) and the SD basis (13.1 ns, Figure 12c) are comparable to each other, despite the $\sqrt{2}$ factor in the NAC used in the SAC calculations. This effect has the same origin as the deviation of the ratio of the timescales in SAC and SD bases from 2 observed for C_3N_4, although it is more severe because the dynamics is even slower than in the C_3N_4 system. To confirm this rationalization, we conduct the calculations using FSSH and ID-A methods (Figure S12). In all cases (except for the ID-A with 14 states), there is an expected factor of 2 acceleration of the dynamics when computed in the SAC basis. Furthermore, we have conducted a systematic scaling of the NACs by the factor $2^{n/2}$ and monitored the ratio of the timescales τ_n computed with the nearby scaling factors, that is τ_n/τ_{n-1} (Figure S13). This approach can be regarded as the comparison of the calculations with SAC and SD bases for different magnitudes of intrinsic NACs. Our expectation is that the ration τ_n/τ_{n-1} should approach 2. We indeed observe this value for n values as low as 3−5. The rate of convergence of the τ_n/τ_{n-1} ratio to 2 depends on the statistics of the sampling. We also consider a longer simulation time for the dynamics, up to 10 ps (up to five times longer), using the repetition of the Hamiltonians that were used for the 2 ps dynamics. In such calculations, the convergence is achieved for smaller n values (e.g., Figure S13b), which indicates that sampling a better statistics of the surface hops (as is in the case of longer trajectories) can reveal the correct scaling of the relaxation rates. We also consider the effect of R^2 value for computing the timescales, that is, we use different tolerances in the fitting procedure to compute the timescales (Figure S13). We observe no significant effect of this parameter.

4. CONCLUSIONS

In this work, we report the development of a new xTB/NA-MD methodology for finite and periodic systems with thousands of atoms. The computational workflow is implemented in the open-source Libra library v5.2.1[133] and leverages the efficient xTB approach as implemented in the CP2K electronic structure package. Through integration with the efficient Libint2 molecular integral library and the use of a sparse matrix format, our Libra workflow enables efficient modeling NA-MD involving hundreds of electronic states of systems with thousands of atoms. As an example, we apply it to model NA-MD in the unprecedentedly large Si NCs with more than 1400 atoms. The approach developed in this work is generalized to compute NACs between bands belonging to distinct *k*-points, although the current tests have been limited to electronic transitions among bands at the same *k*-point.

By modeling the hot electron relaxation dynamics (1.0 eV excess excitation energy) in Si NCs with diameters ranging from 1.2 to 3.5 nm, we find a non-monotonic dependence of carrier relaxation times on the NC diameter in FSSH and mSDM schemes, in agreement with the experimental findings of Bergren et al.[138] The lifetimes vary in the range of 102−133 fs (FSSH), 170−773 (ID-A) fs, and 144−197 (mSDM), reaching maximum for 2.5 nm (FSSH) or 2.8 nm (mSDM) NCs. We attribute the non-monotonic behavior to the interplay of the Si NC size-dependent NAC, which decreases with the NC diameter, and the availability of coherent across-state population-transfer channels, whose number increases in larger NCs. We rationalize the decrease of the NACs in larger NCs by the state localization. On the one hand, when the diameter of Si NCs increases, the "hot" electron states are dominated by the core-localized states, whose effective NACs decrease due to the lower mobility of core atoms. On the other hand, when the diameter of Si NCs increases, the spatial separation of orbitals increases, leading to smaller time−overlaps. We argue that the proper treatment of coherences is needed to obtain the maximum of the carrier relaxation timescales as the function of NC diameter. It is the preservation of coherences that enables population transfer between the non-adjacent but energetically closed states and accelerates the "hot" carrier relaxation in larger systems. The ID-A algorithm destroys the coherences that should be preserved and therefore predicts a monotonic decrease of hot carrier energy relaxation rates with the increase of Si NC diameter.

Our calculations of the nonradiative electron−hole recombination dynamics in periodic 2D (g-C_3N_4) and 3D (MIL-125-NH2 MOF) systems yields the 9.5 and 13.1 ns timescales when computed in the minimal SD basis. These timescales are consistent with the previously reported PBE-based results of Agrawal et al.[161] and Syzgantseva et al.,[86] respectively, as well as with the existing experimental values. In this work, we argue that modeling the nonadiabatic transitions between open- and closed-shell singlet configurations require the use of SACs because it changes the effective NAC by a factor of $\sqrt{2}$ compared to those computed in the bare basis of SDs. This correction leads to 2-fold acceleration of the corresponding processes such as electron−hole recombination dynamics. We also find that modeling the transitions between states coupled by very small NACs (leading to intrinsic timescales > 10 ns) requires careful sampling of the surface hopping statistics, which can be done using either NAC extrapolation or by extending the NA-MD trajectories by repeating the shorter explicitly computed Hamiltonians.

Our assessment of the xTB approach on three types of systems suggests that it yields NACs and overall dynamics comparable to those computed at the DFT/PBE level. We discuss that the short-range nature of the functional causes the gap underestimation in C_3N_4 and Si NC systems and slight overestimation of the gap in the MIL-125-NH2 MOF system compared to those of PBE. At the same time, all the gaps are underestimated compared to experimental values, so the calculations based on these single-particle descriptions of excitations are likely to provide a lower bound to the relaxation timescales. Considering excitonic effects in energy levels, one could expect slower electron−hole recombination dynamics than those computed here. However, as our earlier studies indicate, the excitonic effects also tend to accelerate the dynamics by enhancing mixing of the single-particle states. Assuming these effects negate each other, the timescales computed in this works are likely to be in the correct ballpark, but the exact values can vary.

Finally, in this work, we have assessed several TSH schemes, such as FSSH, ID-A, mSDM, and DISH. The hot carrier relaxation and electron−hole recombination timescales are generally compared as ID-A ≫ DISH > mSDM > FSSH. We observe a qualitative distinction of the ID-A method from all other methods in the systems with multiple intermediate states. While the inclusion of a larger number of intermediate (even higher energy, as in the superexchange model) states accelerates the relaxation dynamics when FSSH, mSDM, and DISH methods are used, the ID-A method predicts a qualitatively opposite behavior. The ID-A algorithm predict the deceleration of the dynamics with more intermediate states added in the model, even if these states are higher in energy than the initial one. We attributed these qualitative differences of the methods to the way they treat coherences. While the FSSH, mSDM, and even DISH methods maintain the coherences between states whose energies evolve nearly parallel in time, the ID-A often removes the coherences between the pairs of states that should remain coherent.

■ ASSOCIATED CONTENT

Supporting Information

The Supporting Information is available free of charge at https://pubs.acs.org/doi/10.1021/acs.jctc.2c00297.

Detailed derivations of results shown in Figure 1, extensive analysis of computations and results of additional computational experiments and convergence studies,evolution of the electron-only excitation energies, probability distribution, isosurfaces, average pure-dephasing times, and dynamics of hot carrier excitation energy relaxation (PDF)

HOMO of Si-NCs (MP4)

LUMO of Si-NCs (MP4)

2D graphitic carbon nitride (MP4)

Detailed scripts and input files used for all types of calculations area available in digital form online at Zenodo server.[137]

■ AUTHOR INFORMATION

Corresponding Author

Alexey V. Akimov − *Department of Chemistry, University at Buffalo, The State University of New York, Buffalo, New York 14260, United States;* orcid.org/0000-0002-7815-3731; Email: alexeyak@buffalo.edu; @AkimovLab

Authors

Mohammad Shakiba − *Department of Chemistry, University at Buffalo, The State University of New York, Buffalo, New York 14260, United States*

Elizabeth Stippell − *Department of Chemistry, University of Southern California, Los Angeles, California 90089, United States*

Wei Li − *School of Chemistry and Materials Science, Hunan Agricultural University, Changsha 410128, China;* orcid.org/0000-0002-9999-5081

Complete contact information is available at:
https://pubs.acs.org/10.1021/acs.jctc.2c00297

Notes

The authors declare no competing financial interest.

■ ACKNOWLEDGMENTS

A.V.A. acknowledges the financial support of the National Science Foundation (Grant OAC-NSF-1931366). Support of computations was provided by the Center for Computational Research at the University at Buffalo.

■ REFERENCES

(1) Shchepanovska, D.; Shannon, R. J.; Curchod, B. F. E.; Glowacki, D. R. Nonadiabatic Kinetics in the Intermediate Coupling Regime: Comparing Molecular Dynamics to an Energy-Grained Master Equation. *J. Phys. Chem. A* **2021**, *125*, 3473−3488.

(2) Toldo, J. M.; do Casal, M. T.; Barbatti, M. Mechanistic Aspects of the Photophysics of UVA Filters Based on Meldrum Derivatives. *J. Phys. Chem. A* **2021**, *125*, 5499−5508.

(3) Curchod, B. F. E.; Rothlisberger, U.; Tavernelli, I. Trajectory-Based Nonadiabatic Dynamics with Time-Dependent Density Functional Theory. *ChemPhysChem* **2013**, *14*, 1314−1340.

(4) Barbatti, M.; Ruckenbauer, M.; Plasser, F.; Pittner, J.; Granucci, G.; Persico, M.; Lischka, H. Newton-X: A Surface-Hopping Program for Nonadiabatic Molecular Dynamics. *Wiley Interdiscip. Rev.: Comput. Mol. Sci.* **2014**, *4*, 26−33.

(5) Curchod, B. F. E.; Penfold, T. J.; Rothlisberger, U.; Tavernelli, I. Local Control Theory in Trajectory Surface Hopping Dynamics Applied to the Excited-State Proton Transfer of 4-Hydroxyacridine. *ChemPhysChem* **2015**, *16*, 2127−2133.

(6) Barbatti, M.; Lischka, H. Nonadiabatic Deactivation of 9H-Adenine: A Comprehensive Picture Based on Mixed Quantum−Classical Dynamics. *J. Am. Chem. Soc.* **2008**, *130*, 6831−6839.

(7) Mukazhanova, A.; Malone, W.; Negrin-Yuvero, H.; Fernandez-Alberti, S.; Tretiak, S.; Sharifzadeh, S. Photoexcitation Dynamics in Perylene Diimide Dimers. *J. Chem. Phys.* **2020**, *153*, 244117.

(8) Song, H.; Nam, Y.; Keefer, D.; Garavelli, M.; Mukamel, S.; Tretiak, S. Nonadiabatic Molecular Dynamics Study of the Relaxation Pathways of Photoexcited Cyclooctatetraene. *J. Phys. Chem. Lett.* **2021**, *12*, 5716−5722.

(9) Zhang, Y.; Nelson, T.; Tretiak, S. Non-Adiabatic Molecular Dynamics of Molecules in the Presence of Strong Light-Matter Interactions. *J. Chem. Phys.* **2019**, *151*, 154109.

(10) Zhang, P.; Hou, Z.; Jiang, L.; Yang, J.; Saidi, W. A.; Prezhdo, O. V.; Li, W. Weak Anharmonicity Rationalizes the Temperature-Driven Acceleration of Nonradiative Dynamics in Cu_2ZnSnS_4 Photo-absorbers. *ACS Appl. Mater. Interfaces* **2021**, *13*, 61365−61373.

(11) He, J.; Fang, W.-H.; Long, R.; Prezhdo, O. V. Why Oxygen Increases Carrier Lifetimes but Accelerates Degradation of $CH_3NH_3PbI_3$ under Light Irradiation: Time-Domain Ab Initio Analysis. *J. Am. Chem. Soc.* **2020**, *142*, 14664−14673.

(12) Sarkar, R.; Kar, M.; Habib, M.; Zhou, G.; Frauenheim, T.; Sarkar, P.; Pal, S.; Prezhdo, O. V. Common Defects Accelerate Charge Separation and Reduce Recombination in CNT/Molecule Composites: Atomistic Quantum Dynamics. *J. Am. Chem. Soc.* **2021**, *143*, 6649−6656.

(13) She, Y.; Hou, Z.; Prezhdo, O. V.; Li, W. Identifying and Passivating Killer Defects in Pb-Free Double $Cs_2AgBiBr_6$ Perovskite. *J. Phys. Chem. Lett.* **2021**, *12*, 10581−10588.

(14) Li, W.; Zhou, L.; Prezhdo, O. V.; Akimov, A. V. Spin−Orbit Interactions Greatly Accelerate Nonradiative Dynamics in Lead Halide Perovskites. *ACS Energy Lett.* **2018**, *3*, 2159−2166.

(15) Yazdani, N.; Bozyigit, D.; Vuttivorakulchai, K.; Luisier, M.; Infante, I.; Wood, V. Tuning Electron−Phonon Interactions in Nanocrystals through Surface Termination. *Nano Lett.* **2018**, *18*, 2233−2242.

(16) Boehme, S. C.; Brinck, S. t.; Maes, J.; Yazdani, N.; Zapata, F.; Chen, K.; Wood, V.; Hodgkiss, J. M.; Hens, Z.; Geiregat, P.; Infante, I. Phonon-Mediated and Weakly Size-Dependent Electron and Hole Cooling in $CsPbBr_3$ Nanocrystals Revealed by Atomistic Simulations and Ultrafast Spectroscopy. *Nano Lett.* **2020**, *20*, 1819−1829.

(17) Grimaldi, G.; Crisp, R. W.; ten Brinck, S.; Zapata, F.; van Ouwendorp, M.; Renaud, N.; Kirkwood, N.; Evers, W. H.; Kinge, S.; Infante, I.; Siebbeles, L. D. A.; Houtepen, A. J. Hot-Electron Transfer in Quantum-Dot Heterojunction Films. *Nat. Commun.* **2018**, *9*, 2310.

(18) Wang, H. I.; Infante, I.; Brinck, S. t.; Cánovas, E.; Bonn, M. Efficient Hot Electron Transfer in Quantum Dot-Sensitized Mesoporous Oxides at Room Temperature. *Nano Lett.* **2018**, *18*, 5111−5115.

(19) Forde, A.; Kilin, D. Defect Tolerance Mechanism Revealed! Influence of Polaron Occupied Surface Trap States on $CsPbBr_3$ Nanocrystal Photoluminescence: Ab Initio Excited-State Dynamics. *J. Chem. Theory Comput.* **2021**, *17*, 7224−7236.

(20) Han, Y.; Kilin, D. S. Nonradiative Relaxation Dynamics of a Cesium Lead Halide Perovskite Photovoltaic Architecture: Effect of External Electric Fields. *J. Phys. Chem. Lett.* **2020**, *11*, 9983−9989.

(21) Lystrom, L.; Tamukong, P.; Mihaylov, D.; Kilina, S. Phonon-Driven Energy Relaxation in PbS/CdS and PbSe/CdSe Core/Shell Quantum Dots. *J. Phys. Chem. Lett.* **2020**, *11*, 4269−4278.

(22) Kilina, S.; Velizhanin, K. A.; Ivanov, S.; Prezhdo, O. V.; Tretiak, S. Surface Ligands Increase Photoexcitation Relaxation Rates in CdSe Quantum Dots. *ACS Nano* **2012**, *6*, 6515−6524.

(23) Chu, W.; Zheng, Q.; Prezhdo, O. V.; Zhao, J.; Saidi, W. A. Low-Frequency Lattice Phonons in Halide Perovskites Explain High Defect Tolerance toward Electron-Hole Recombination. *Sci. Adv.* **2020**, *6*, No. eaaw7453.

(24) Jiang, X.; Zheng, Q.; Lan, Z.; Saidi, W. A.; Ren, X.; Zhao, J. Real-Time GW-BSE Investigations on Spin-Valley Exciton Dynamics in Monolayer Transition Metal Dichalcogenide. *Sci. Adv.* **2021**, *7*, No. eabf3759.

(25) Trivedi, D. J.; Wang, L.; Prezhdo, O. V. Auger-Mediated Electron Relaxation Is Robust to Deep Hole Traps: Time-Domain Ab Initio Study of CdSe Quantum Dots. *Nano Lett.* **2015**, *15*, 2086−2091.

(26) Li, W.; Zhang, X.; Lu, G. Unraveling Photoexcitation Dynamics at "Dots-in-a-Perovskite" Heterojunctions from First-Principles. *J. Mater. Chem. A* **2019**, *7*, 18012−18019.

(27) Madjet, M. E.; Berdiyorov, G. R.; El-Mellouhi, F.; Alharbi, F. H.; Akimov, A. V.; Kais, S. Cation Effect on Hot Carrier Cooling in Halide Perovskite Materials. *J. Phys. Chem. Lett.* **2017**, *8*, 4439−4445.

(28) Smith, B.; Akimov, A. V. Hot Electron Cooling in Silicon Nanoclusters via Landau−Zener Nonadiabatic Molecular Dynamics: Size Dependence and Role of Surface Termination. *J. Phys. Chem. Lett.* **2020**, *11*, 1456−1465.

(29) Smith, B.; Shakiba, M.; Akimov, A. V. Nonadiabatic Dynamics in Si and CdSe Nanoclusters: Many-Body vs Single-Particle Treatment of Excited States. *J. Chem. Theory Comput.* **2021**, *17*, 678−693.

(30) Smith, B.; Shakiba, M.; Akimov, A. V. Crystal Symmetry and Static Electron Correlation Greatly Accelerate Nonradiative Dynamics in Lead Halide Perovskites. *J. Phys. Chem. Lett.* **2021**, *12*, 2444−2453.

(31) Chu, W.; Saidi, W. A.; Zhao, J.; Prezhdo, O. V. Soft Lattice and Defect Covalency Rationalize Tolerance of β-$CsPbI_3$ Perovskite Solar Cells to Native Defects. *Angew. Chem., Int. Ed.* **2020**, *59*, 6435−6441.

(32) Ha, Y.; Park, J.-G.; Hong, K.-H.; Kim, H. Enhanced Light Emission through Symmetry Engineering of Halide Perovskites. *J. Am. Chem. Soc.* **2022**, *144*, 297−305.

(33) Cheng, C.; Fang, W.-H.; Long, R.; Prezhdo, O. V. Water Splitting with a Single-Atom Cu/TiO_2 Photocatalyst: Atomistic Origin of High Efficiency and Proposed Enhancement by Spin Selection. *JACS Au* **2021**, *1*, 550−559.

(34) Akimov, A. V.; Asahi, R.; Jinnouchi, R.; Prezhdo, O. V. What Makes the Photocatalytic CO_2 Reduction on N-Doped Ta_2O_5 Efficient: Insights from Nonadiabatic Molecular Dynamics. *J. Am. Chem. Soc.* **2015**, *137*, 11517−11525.

(35) Akimov, A. V.; Neukirch, A. J.; Prezhdo, O. V. Theoretical Insights into Photoinduced Charge Transfer and Catalysis at Oxide Interfaces. *Chem. Rev.* **2013**, *113*, 4496−4565.

(36) Niu, X.; Bai, X.; Zhou, Z.; Wang, J. Rational Design and Characterization of Direct Z-Scheme Photocatalyst for Overall Water Splitting from Excited State Dynamics Simulations. *ACS Catal.* **2020**, *10*, 1976−1983.

(37) Nam, Y.; Li, L.; Lee, J. Y.; Prezhdo, O. V. Size and Shape Effects on Charge Recombination Dynamics of TiO_2 Nanoclusters. *J. Phys. Chem. C* **2018**, *122*, 5201−5208.

(38) Reeves, K. G.; Schleife, A.; Correa, A. A.; Kanai, Y. Role of Surface Termination on Hot Electron Relaxation in Silicon Quantum Dots: A First-Principles Dynamics Simulation Study. *Nano Lett.* **2015**, *15*, 6429−6433.

(39) Liu, J.; Neukirch, A. J.; Prezhdo, O. V. Non-Radiative Electron−Hole Recombination in Silicon Clusters: Ab Initio Non-Adiabatic Molecular Dynamics. *J. Phys. Chem. C* **2014**, *118*, 20702−20709.

(40) Seifert, G.; Porezag, D.; Frauenheim, T. Calculations of Molecules, Clusters, and Solids with a Simplified LCAO-DFT-LDA Scheme. *Int. J. Quantum Chem.* **1996**, *58*, 185−192.

(41) Elstner, M.; Porezag, D.; Jungnickel, G.; Elsner, J.; Haugk, M.; Frauenheim, T.; Suhai, S.; Seifert, G. Self-Consistent-Charge Density-Functional Tight-Binding Method for Simulations of Complex Materials Properties. *Phys. Rev. B: Condens. Matter Mater. Phys.* **1998**, *58*, 7260−7268.

(42) Aradi, B.; Hourahine, B.; Frauenheim, T. DFTB+, a Sparse Matrix-Based Implementation of the DFTB Method. *J. Phys. Chem. A* **2007**, *111*, 5678−5684.

(43) Hourahine, B.; Aradi, B.; Blum, V.; Bonafé, F.; Buccheri, A.; Camacho, C.; Cevallos, C.; Deshaye, M. Y.; Dumitrică, T.; Dominguez, A.; Ehlert, S.; Elstner, M.; van der Heide, T.; Hermann, J.; Irle, S.; Kranz, J. J.; Köhler, C.; Kowalczyk, T.; Kubař, T.; Lee, I. S.; Lutsker, V.; Maurer, R. J.; Min, S. K.; Mitchell, I.; Negre, C.; Niehaus, T. A.; Niklasson, A. M. N.; Page, A. J.; Pecchia, A.; Penazzi, G.; Persson, M. P.; Řezáč, J.; Sánchez, C. G.; Sternberg, M.; Stöhr, M.; Stuckenberg, F.; Tkatchenko, A.; Yu, V. W.-z.; Frauenheim, T. DFTB+, a Software Package for Efficient Approximate Density Functional Theory Based Atomistic Simulations. *J. Chem. Phys.* **2020**, *152*, 124101.

(44) Komoto, N.; Yoshikawa, T.; Nishimura, Y.; Nakai, H. Large-Scale Molecular Dynamics Simulation for Ground and Excited States Based on Divide-and-Conquer Long-Range Corrected Density-Functional Tight-Binding Method. *J. Chem. Theory Comput.* **2020**, *16*, 2369−2378.

(45) Uratani, H.; Nakai, H. Scalable Ehrenfest Molecular Dynamics Exploiting the Locality of Density-Functional Tight-Binding Hamiltonian. *J. Chem. Theory Comput.* **2021**, *17*, 7384−7396.

(46) Dewar, M. J. S.; Zoebisch, E. G.; Healy, E. F.; Stewart, J. J. P. Development and Use of Quantum Mechanical Molecular Models. 76. AM1: A New General Purpose Quantum Mechanical Molecular Model. *J. Am. Chem. Soc.* **1985**, *107*, 3902−3909.

(47) Stewart, J. J. P. Optimization of Parameters for Semiempirical Methods I. Method. *J. Comput. Chem.* **1989**, *10*, 209−220.

(48) Dewar, M. J. S.; Thiel, W. Ground States of Molecules. 38. The MNDO Method. Approximations and Parameters. *J. Am. Chem. Soc.* **1977**, *99*, 4899−4907.

(49) Malone, W.; Nebgen, B.; White, A.; Zhang, Y.; Song, H.; Bjorgaard, J. A.; Sifain, A. E.; Rodriguez-Hernandez, B.; Freixas, V. M.; Fernandez-Alberti, S.; Roitberg, A. E.; Nelson, T. R.; Tretiak, S. NEXMD Software Package for Nonadiabatic Excited State Molecular Dynamics Simulations. *J. Chem. Theory Comput.* **2020**, *16*, 5771−5783.

(50) Nelson, T. R.; White, A. J.; Bjorgaard, J. A.; Sifain, A. E.; Zhang, Y.; Nebgen, B.; Fernandez-Alberti, S.; Mozyrsky, D.; Roitberg, A. E.; Tretiak, S. Non-Adiabatic Excited-State Molecular Dynamics: Theory and Applications for Modeling Photophysics in Extended Molecular Materials. *Chem. Rev.* **2020**, *120*, 2215−2287.

(51) Zerner, M. C.; Loew, G. H.; Kirchner, R. F.; Mueller-Westerhoff, U. T. An Intermediate Neglect of Differential Overlap Technique for Spectroscopy of Transition-Metal Complexes. Ferrocene. *J. Am. Chem. Soc.* **1980**, *102*, 589−599.

(52) Field, M. J.; Bash, P. A.; Karplus, M. A Combined Quantum Mechanical and Molecular Mechanical Potential for Molecular Dynamics Simulations. *J. Comput. Chem.* **1990**, *11*, 700−733.

(53) Senn, H. M.; Thiel, W. QM/MM Methods for Biomolecular Systems. *Angew. Chem., Int. Ed.* **2009**, *48*, 1198−1229.

(54) Akimov, A. V. Nonadiabatic Molecular Dynamics with Tight-Binding Fragment Molecular Orbitals. *J. Chem. Theory Comput.* **2016**, *12*, 5719−5736.

(55) Spencer, J.; Gajdos, F.; Blumberger, J. FOB-SH: Fragment orbital-based surface hopping for charge carrier transport in organic and biological molecules and materials. *J. Chem. Phys.* **2016**, *145*, 064102.

(56) Genova, A.; Ceresoli, D.; Krishtal, A.; Andreussi, O.; DiStasio, R. A., Jr.; Pavanello, M. eQE An Open-Source Density Functional Embedding Theory Code for the Condensed Phase. *Int. J. Quantum Chem.* **2017**, *117*, No. e25401.

(57) Fedorov, D. G.; Nakamura, T. Free Energy Decomposition Analysis Based on the Fragment Molecular Orbital Method. *J. Phys. Chem. Lett.* **2022**, *13*, 1596−1601.

(58) Jia, W.; Wang, J.; Chi, X.; Wang, L.-W. GPU Implementation of the Linear Scaling Three Dimensional Fragment Method for Large Scale Electronic Structure Calculations. *Comput. Phys. Commun.* **2017**, *211*, 8−15.

(59) Wang, L.-W.; Zhao, Z.; Meza, J. Linear-Scaling Three-Dimensional Fragment Method for Large-Scale Electronic Structure Calculations. *Phys. Rev. B: Condens. Matter Mater. Phys.* **2008**, *77*, 165113.

(60) Yoshikawa, T.; Kobayashi, M.; Nakai, H. Divide-and-Conquer-Based Symmetry Adapted Cluster Method: Synergistic Effect of Subsystem Fragmentation and Configuration Selection. *Int. J. Quantum Chem.* **2013**, *113*, 218−223.

(61) Kobayashi, M.; Nakai, H. How Does It Become Possible to Treat Delocalized and/or Open-Shell Systems in Fragmentation-Based Linear-Scaling Electronic Structure Calculations? The Case of the Divide-and-Conquer Method. *Phys. Chem. Chem. Phys.* **2012**, *14*, 7629−7639.

(62) Zobel, J. P.; Heindl, M.; Plasser, F.; Mai, S.; González, L. Surface Hopping Dynamics on Vibronic Coupling Models. *Acc. Chem. Res.* **2021**, *54*, 3760−3771.

(63) Belyaev, A. K.; Lebedev, O. V. Nonadiabatic Nuclear Dynamics of Atomic Collisions Based on Branching Classical Trajectories. *Phys. Rev. A* **2011**, *84*, 014701.

(64) Baeck, K. K.; An, H. Practical Approximation of the Non-Adiabatic Coupling Terms for Same-Symmetry Interstate Crossings by Using Adiabatic Potential Energies Only. *J. Chem. Phys.* **2017**, *146*, 064107.

(65) do Casal, M. T.; Pinheiro, M.; Barbatti, M., Jr.; Barbatti, M. Fewest Switches Surface Hopping with Baeck-An Couplings. *Open Res. Europe* **2022**, *1*, 49.

(66) Nakamura, T.; Yokaichiya, T.; Fedorov, D. G. Quantum-Mechanical Structure Optimization of Protein Crystals and Analysis of Interactions in Periodic Systems. *J. Phys. Chem. Lett.* **2021**, *12*, 8757−8762.

(67) Ehrlich, S.; Göller, A. H.; Grimme, S. Towards Full Quantum-Mechanics-Based Protein−Ligand Binding Affinities. *ChemPhysChem* **2017**, *18*, 898−905.

(68) Zuehlsdorff, T. J.; Napoli, J. A.; Milanese, J. M.; Markland, T. E.; Isborn, C. M. Unraveling Electronic Absorption Spectra Using Nuclear Quantum Effects: Photoactive Yellow Protein and Green Fluorescent Protein Chromophores in Water. *J. Chem. Phys.* **2018**, *149*, 024107.

(69) Pal, S.; Casanova, D.; Prezhdo, O. V. Effect of Aspect Ratio on Multiparticle Auger Recombination in Single-Walled Carbon Nanotubes: Time Domain Atomistic Simulation. *Nano Lett.* **2018**, *18*, 58−63.

(70) Kruse, H.; Banáš, P.; Šponer, J. Investigations of Stacked DNA Base-Pair Steps: Highly Accurate Stacking Interaction Energies, Energy Decomposition, and Many-Body Stacking Effects. *J. Chem. Theory Comput.* **2019**, *15*, 95−115.

(71) Stojanović, L.; Aziz, S. G.; Hilal, R. H.; Plasser, F.; Niehaus, T. A.; Barbatti, M. Nonadiabatic Dynamics of Cycloparaphenylenes with TD-DFTB Surface Hopping. *J. Chem. Theory Comput.* **2017**, *13*, 5846−5860.

(72) Bannwarth, C.; Caldeweyher, E.; Ehlert, S.; Hansen, A.; Pracht, P.; Seibert, J.; Spicher, S.; Grimme, S. Extended Tight-Binding Quantum Chemistry Methods. *Wiley Interdiscip. Rev.: Comput. Mol. Sci.* **2021**, *11*, No. e1493.

(73) Bannwarth, C.; Ehlert, S.; Grimme, S. GFN2-XTB—An Accurate and Broadly Parametrized Self-Consistent Tight-Binding Quantum Chemical Method with Multipole Electrostatics and Density-Dependent Dispersion Contributions. *J. Chem. Theory Comput.* **2019**, *15*, 1652−1671.

(74) Grimme, S.; Bannwarth, C.; Shushkov, P. A Robust and Accurate Tight-Binding Quantum Chemical Method for Structures, Vibrational Frequencies, and Noncovalent Interactions of Large Molecular Systems Parametrized for All Spd-Block Elements (Z = 1−86). *J. Chem. Theory Comput.* **2017**, *13*, 1989−2009.

(75) Hutter, J.; Iannuzzi, M.; Schiffmann, F.; VandeVondele, J. CP2K: Atomistic Simulations of Condensed Matter Systems. *Wiley Interdiscip. Rev.: Comput. Mol. Sci.* **2014**, *4*, 15−25.

(76) Kühne, T. D.; Iannuzzi, M.; Del Ben, M.; Rybkin, V. V.; Seewald, P.; Stein, F.; Laino, T.; Khaliullin, R. Z.; Schütt, O.; Schiffmann, F.; Golze, D.; Wilhelm, J.; Chulkov, S.; Bani-Hashemian, M. H.; Weber, V.; Borštnik, U.; Taillefumier, M.; Jakobovits, A. S.; Lazzaro, A.; Pabst, H.; Müller, T.; Schade, R.; Guidon, M.; Andermatt, S.; Holmberg, N.; Schenter, G. K.; Hehn, A.; Bussy, A.; Belleflamme, F.; Tabacchi, G.; Glöß, A.; Lass, M.; Bethune, I.; Mundy, C. J.; Plessl, C.; Watkins, M.; VandeVondele, J.; Krack, M.; Hutter, J. CP2K: An Electronic Structure and Molecular Dynamics Software Package - Quickstep: Efficient and Accurate Electronic Structure Calculations. *J. Chem. Phys.* **2020**, *152*, 194103.

(77) Neese, F. Software Update: The ORCA Program System, Version 4.0. *Wiley Interdiscip. Rev.: Comput. Mol. Sci.* **2018**, *8*, No. e1327.

(78) Seritan, S.; Bannwarth, C.; Fales, B. S.; Hohenstein, E. G.; Isborn, C. M.; Kokkila-Schumacher, S. I. L.; Li, X.; Liu, F.; Luehr, N.; Snyder, J. W., Jr.; Song, C.; Titov, A. V.; Ufimtsev, I. S.; Wang, L.-P.; Martínez, T. J. TeraChem: A Graphical Processing Unit-Accelerated Electronic Structure Package for Large-Scale Ab Initio Molecular Dynamics. *Wiley Interdiscip. Rev.: Comput. Mol. Sci.* **2021**, *11*, No. e1494.

(79) Balasubramani, S. G.; Chen, G. P.; Coriani, S.; Diedenhofen, M.; Frank, M. S.; Franzke, Y. J.; Furche, F.; Grotjahn, R.; Harding, M. E.; Hättig, C.; Hellweg, A.; Helmich-Paris, B.; Holzer, C.; Huniar, U.; Kaupp, M.; Marefat Khah, A.; Karbalaei Khani, S.; Müller, T.; Mack, F.; Nguyen, B. D.; Parker, S. M.; Perlt, E.; Rappoport, D.; Reiter, K.; Roy, S.; Rückert, M.; Schmitz, G.; Sierka, M.; Tapavicza, E.; Tew, D. P.; van Wüllen, C.; Voora, V. K.; Weigend, F.; Wodyński, A.; Yu, J. M. TURBOMOLE: Modular Program Suite for *Ab Initio* Quantum-Chemical and Condensed-Matter Simulations. *J. Chem. Phys.* **2020**, *152*, 184107.

(80) Shen, J.; He, X.; Ke, T.; Krishna, R.; van Baten, J. M.; Chen, R.; Bao, Z.; Xing, H.; Dincă, M.; Zhang, Z.; Yang, Q.; Ren, Q. Simultaneous Interlayer and Intralayer Space Control in Two-Dimensional Metal−organic Frameworks for Acetylene/Ethylene Separation. *Nat. Commun.* **2020**, *11*, 6259.

(81) Saura-Sanmartin, A.; Martinez-Cuezva, A.; Marin-Luna, M.; Bautista, D.; Berna, J. Effective Encapsulation of C_{60} by Metal−Organic Frameworks with Polyamide Macrocyclic Linkers. *Angew. Chem.* **2021**, *133*, 10909−10914.

(82) Schmitz, S.; Seibert, J.; Ostermeir, K.; Hansen, A.; Göller, A. H.; Grimme, S. Quantum Chemical Calculation of Molecular and Periodic Peptide and Protein Structures. *J. Phys. Chem. B* **2020**, *124*, 3636−3646.

(83) Yepes, D.; Neese, F.; List, B.; Bistoni, G. Unveiling the Delicate Balance of Steric and Dispersion Interactions in Organocatalysis Using High-Level Computational Methods. *J. Am. Chem. Soc.* **2020**, *142*, 3613−3625.

(84) Li, X.; Deng, Y.; Lai, J.; Zhao, G.; Dong, S. Tough, Long-Term, Water-Resistant, and Underwater Adhesion of Low-Molecular-Weight Supramolecular Adhesives. *J. Am. Chem. Soc.* **2020**, *142*, 5371−5379.

(85) Frisch, M. J.; Trucks, G. W.; Schlegel, H. B.; Scuseria, G. E.; Robb, M. A.; Cheeseman, J. R.; Scalmani, G.; Barone, V.; Mennucci, B.; Petersson, G. A.; Nakatsuji, H.; Caricato, M.; Li, X.; Hratchian, H. P.; Izmaylov, A. F.; Bloino, J.; Zheng, G.; Sonnenberg, J. L.; Hada, M.; Ehara, M.; Toyota, K.; Fukuda, R.; Hasegawa, J.; Ishida, M.; Nakajima, T.; Honda, Y.; Kitao, O.; Nakai, H.; Vreven, T.; Montgomery, J. A., Jr.; Peralta, J. E.; Ogliaro, F.; Bearpark, M.; Heyd, J. J.; Brothers, E.; Kudin, K. N.; Staroverov, V. N.; Kobayashi, R.; Normand, J.; Raghavachari, K.; Rendell, A.; Burant, J. C.; Iyengar, S. S.; Tomasi, J.; Cossi, M.; Rega, N.; Millam, J. M.; Klene, M.; Knox, J. E.; Cross, J. B.; Bakken, V.; Adamo, C.; Jaramillo, J.; Gomperts, R.; Stratmann, R. E.; Yazyev, O.; Austin, A. J.; Cammi, R.; Pomelli, C.; Ochterski, J. W.; Martin, R. L.; Morokuma, K.; Zakrzewski, V. G.; Voth, G. A.; Salvador, P.; Dannenberg, J. J.; Dapprich, S.; Daniels, A. D.; Farkas, O.; Foresman, J. B.; Ortiz, J. V.; Cioslowski, J.; Fox, D. J. *Gaussian 09*, Revision D.01; Gaussian, Inc., 2009.

(86) Syzgantseva, M. A.; Syzgantseva, O. A. Efficient Computation of Nonadiabatic Coupling Coefficients for Modeling Charge Carrier Recombination in Extended Systems: The Case of Metal−Organic Frameworks. *J. Phys. Chem. A* **2021**, *125*, 9700−9706.

(87) Mai, S.; Marquetand, P.; González, L. Nonadiabatic Dynamics: The SHARC Approach. *Wiley Interdiscip. Rev.: Comput. Mol. Sci.* **2018**, *8*, No. e1370.

(88) Plasser, F.; Ruckenbauer, M.; Mai, S.; Oppel, M.; Marquetand, P.; González, L. Efficient and Flexible Computation of Many-Electron Wave Function Overlaps. *J. Chem. Theory Comput.* **2016**, *12*, 1207−1219.

(89) Akimov, A. V. Libra: An Open-Source "Methodology Discovery" Library for Quantum and Classical Dynamics Simulations. *J. Comput. Chem.* **2016**, *37*, 1626−1649.

(90) Valeev, E. F. *Libint: A Library for the Evaluation of Molecular Integrals of Many-Body Operators over Gaussian Functions*, Version 2.6.0. http://libint.valeyev.net (accessed June 8, 2022).

(91) Carey, G. H.; Abdelhady, A. L.; Ning, Z.; Thon, S. M.; Bakr, O. M.; Sargent, E. H. Colloidal Quantum Dot Solar Cells. *Chem. Rev.* **2015**, *115*, 12732−12763.

(92) Zhao, H.; Rosei, F. Colloidal Quantum Dots for Solar Technologies. *Chem* **2017**, *3*, 229−258.

(93) Sargent, E. H. Colloidal Quantum Dot Solar Cells. *Nat. Photonics* **2012**, *6*, 133−135.

(94) Zhou, J.; Huang, J.; Chen, H.; Samanta, A.; Linnros, J.; Yang, Z.; Sychugov, I. Low-Cost Synthesis of Silicon Quantum Dots with Near-Unity Internal Quantum Efficiency. *J. Phys. Chem. Lett.* **2021**, *12*, 8909−8916.

(95) Dutta, M.; Thirugnanam, L.; Trinh, P. V.; Fukata, N. High Efficiency Hybrid Solar Cells Using Nanocrystalline Si Quantum Dots and Si Nanowires. *ACS Nano* **2015**, *9*, 6891−6899.

(96) Dohnalová, K.; Gregorkiewicz, T.; Kůsová, K. Silicon Quantum Dots: Surface Matters. *J. Phys.: Condens. Matter* **2014**, *26*, 173201.

(97) Wang, X.; Maeda, K.; Thomas, A.; Takanabe, K.; Xin, G.; Carlsson, J. M.; Domen, K.; Antonietti, M. A Metal-Free Polymeric Photocatalyst for Hydrogen Production from Water under Visible Light. *Nat. Mater.* **2009**, *8*, 76−80.

(98) Zhao, G.; Yang, H.; Liu, M.; Xu, X. Metal-Free Graphitic Carbon Nitride Photocatalyst Goes Into Two-Dimensional Time. *Front. Chem.* **2018**, *6*, 551.

(99) Praus, P. A Brief Review of S-Triazine Graphitic Carbon Nitride. *Carbon Lett.* **2022**, *32*, 703.

(100) Dan-Hardi, M.; Serre, C.; Frot, T.; Rozes, L.; Maurin, G.; Sanchez, C.; Férey, G. A New Photoactive Crystalline Highly Porous Titanium (IV) Dicarboxylate. *J. Am. Chem. Soc.* **2009**, *131*, 10857−10859.

(101) Lee, Y.; Kim, S.; Kang, J. K.; Cohen, S. M. Photocatalytic CO_2 Reduction by a Mixed Metal (Zr/Ti), Mixed Ligand Metal−Organic Framework under Visible Light Irradiation. *Chem. Commun.* **2015**, *51*, 5735−5738.

(102) Santaclara, J. G.; Nasalevich, M. A.; Castellanos, S.; Evers, W. H.; Spoor, F. C. M.; Rock, K.; Siebbeles, L. D. A.; Kapteijn, F.; Grozema, F.; Houtepen, A.; Gascon, J.; Hunger, J.; van der Veen, M. A. Organic Linker Defines the Excited-State Decay of Photocatalytic MIL-125(Ti)-Type Materials. *ChemSusChem* **2016**, *9*, 388−395.

(103) Syzgantseva, M. A.; Stepanov, N. F.; Syzgantseva, O. A. Band Alignment as the Method for Modifying Electronic Structure of Metal- Organic Frameworks. *ACS Appl. Mater. Interfaces* **2020**, *12*, 17611−17619.

(104) Smith, B.; Akimov, A. V. Modeling Nonadiabatic Dynamics in Condensed Matter Materials: Some Recent Advances and Applications. *J. Phys.: Condens. Matter* **2019**, *32*, 073001.

(105) Curchod, B. F. E.; Martínez, T. J. Ab Initio Nonadiabatic Quantum Molecular Dynamics. *Chem. Rev.* **2018**, *118*, 3305−3336.

(106) Prezhdo, O. V. Modeling Non-Adiabatic Dynamics in Nanoscale and Condensed Matter Systems. *Acc. Chem. Res.* **2021**, *54*, 4239−4249.

(107) Crespo-Otero, R.; Barbatti, M. Recent Advances and Perspectives on Nonadiabatic Mixed Quantum−Classical Dynamics. *Chem. Rev.* **2018**, *118*, 7026−7068.

(108) Tully, J. C. Molecular Dynamics with Electronic Transitions. *J. Chem. Phys.* **1990**, *93*, 1061−1071.

(109) Craig, C. F.; Duncan, W. R.; Prezhdo, O. V. Trajectory Surface Hopping in the Time-Dependent Kohn-Sham Approach for Electron-Nuclear Dynamics. *Phys. Rev. Lett.* **2005**, *95*, 163001.

(110) Duncan, W. R.; Craig, C. F.; Prezhdo, O. V. Time-Domain Ab Initio Study of Charge Relaxation and Recombination in Dye-Sensitized TiO_2. *J. Am. Chem. Soc.* **2007**, *129*, 8528−8543.

(111) Prezhdo, O. V.; Duncan, W. R.; Prezhdo, V. V. Photoinduced Electron Dynamics at the Chromophore−Semiconductor Interface: A Time-Domain Ab Initio Perspective. *Prog. Surf. Sci.* **2009**, *84*, 30−68.

(112) Uratani, H.; Nakai, H. Simulating the Coupled Structural−Electronic Dynamics of Photo-Excited Lead Iodide Perovskites. *J. Phys. Chem. Lett.* **2020**, *11*, 4448−4455.

(113) Plasser, F.; Mai, S.; Fumanal, M.; Gindensperger, E.; Daniel, C.; González, L. Strong Influence of Decoherence Corrections and Momentum Rescaling in Surface Hopping Dynamics of Transition Metal Complexes. *J. Chem. Theory Comput.* **2019**, *15*, 5031−5045.

(114) Nelson, T.; Fernandez-Alberti, S.; Roitberg, A. E.; Tretiak, S. Nonadiabatic Excited-State Molecular Dynamics: Treatment of Electronic Decoherence. *J. Chem. Phys.* **2013**, *138*, 224111.

(115) Smith, B.; Akimov, A. V. A Comparative Analysis of Surface Hopping Acceptance and Decoherence Algorithms within the Neglect of Back-Reaction Approximation. *J. Chem. Phys.* **2019**, *151*, 124107.

(116) Granucci, G.; Persico, M. Critical Appraisal of the Fewest Switches Algorithm for Surface Hopping. *J. Chem. Phys.* **2007**, *126*, 134114.

(117) Jaeger, H. M.; Fischer, S.; Prezhdo, O. V. Decoherence-Induced Surface Hopping. *J. Chem. Phys.* **2012**, *137*, 22A545.

(118) Akimov, A. V. Excited State Dynamics in Monolayer Black Phosphorus Revisited: Accounting for Many-Body Effects. *J. Chem. Phys.* **2021**, *155*, 134106.

(119) Akimov, A. V.; Prezhdo, O. V. Persistent Electronic Coherence Despite Rapid Loss of Electron−Nuclear Correlation. *J. Phys. Chem. Lett.* **2013**, *4*, 3857−3864.

(120) Hammes-Schiffer, S.; Tully, J. C. Proton Transfer in Solution: Molecular Dynamics with Quantum Transitions. *J. Chem. Phys.* **1994**, *101*, 4657−4667.

(121) Senanayake, R. D.; Aikens, C. M. Theoretical Investigation of Relaxation Dynamics in the $Au_{18}(SH)_{14}$ Thiolate-Protected Gold Nanocluster. *J. Chem. Phys.* **2019**, *151*, 094702.

(122) Senanayake, R. D.; Aikens, C. M. Electronic Relaxation Dynamics in $[Au_{25}(SR)_{18}]^{-1}$ (R= CH_3, C_2H_5, C_3H_7, MPA, PET) Thiolate-Protected Nanoclusters. *Phys. Chem. Chem. Phys.* **2020**, *22*, 5272−5285.

(123) Ziogos, O. G.; Blumberger, J. Ultrafast Estimation of Electronic Couplings for Electron Transfer between Pi-Conjugated Organic Molecules. II. *J. Chem. Phys.* **2021**, *155*, 244110.

(124) Giannini, S.; Blumberger, J. Charge Transport in Organic Semiconductors: The Perspective from Nonadiabatic Molecular Dynamics. *Acc. Chem. Res.* **2022**, *55*, 819−830.

(125) Akimov, A. V.; Prezhdo, O. V. The PYXAID Program for Non-Adiabatic Molecular Dynamics in Condensed Matter Systems. *J. Chem. Theory Comput.* **2013**, *9*, 4959−4972.

(126) Akimov, A. V.; Prezhdo, O. V. Advanced Capabilities of the PYXAID Program: Integration Schemes, Decoherence Effects, Multiexcitonic States, and Field-Matter Interaction. *J. Chem. Theory Comput.* **2014**, *10*, 789−804.

(127) Pal, S.; Trivedi, D. J.; Akimov, A. V.; Aradi, B.; Frauenheim, T.; Prezhdo, O. V. Nonadiabatic Molecular Dynamics for Thousand Atom Systems: A Tight-Binding Approach toward PYXAID. *J. Chem. Theory Comput.* **2016**, *12*, 1436−1448.

(128) Ryabinkin, I. G.; Izmaylov, A. F. Mixed Quantum-Classical Dynamics Using Collective Electronic Variables: A Better Alternative to Electronic Friction Theories. *J. Phys. Chem. Lett.* **2017**, *8*, 440−444.

(129) Ryabinkin, I. G.; Joubert-Doriol, L.; Izmaylov, A. F. Geometric Phase Effects in Nonadiabatic Dynamics near Conical Intersections. *Acc. Chem. Res.* **2017**, *50*, 1785−1793.

(130) Fernandez-Alberti, S.; Roitberg, A. E.; Nelson, T.; Tretiak, S. Identification of Unavoided Crossings in Nonadiabatic Photoexcited Dynamics Involving Multiple Electronic States in Polyatomic Conjugated Molecules. *J. Chem. Phys.* **2012**, *137*, 014512.

(131) Temen, S.; Akimov, A. V. A Simple Solution to Trivial Crossings: A Stochastic State Tracking Approach. *J. Phys. Chem. Lett.* **2021**, *12*, 850−860.

(132) Akimov, A. V. A Simple Phase Correction Makes a Big Difference in Nonadiabatic Molecular Dynamics. *J. Phys. Chem. Lett.* **2018**, *9*, 6096−6102.

(133) Akimov, A. V.; Shakiba, M.; Smith, B.; Sato, K.; Dutra, M.; Temen, S.; Li, W.; Sun, X.; Stippell, L.; Chan, M. *Quantum-Dynamics-Hub/libra-code: Revised xTB/Libra Workflow*, (v5.2.1); Zenodo, 2022. https://doi.org/10.5281/zenodo.6615255 (accessed June 8, 2022).

(134) Schaftenaar, G.; Noordik, J. H. Molden: A Pre-and Post-Processing Program for Molecular and Electronic Structures. *J. Comput.-Aided Mol. Des.* **2000**, *14*, 123−134.

(135) Zapata, F.; Ridder, L.; Hidding, J.; Jacob, C. R.; Infante, I.; Visscher, L. QMflows: A Tool Kit for Interoperable Parallel Workflows in Quantum Chemistry. *J. Chem. Inf. Model.* **2019**, *59*, 3191−3197.

(136) Humphrey, W.; Dalke, A.; Schulten, K. VMD: Visual Molecular Dynamics. *J. Mol. Graph.* **1996**, *14*, 33−38.

(137) Shakiba, M.; Akimov, A. V. *AkimovLab/Project_Libra-xTB: Revised xTB/Libra Project Repository*, (v2.0.0); Zenodo, 2022. https://doi.org/10.5281/zenodo.6615218 (accessed June 8, 2022).

(138) Bergren, M. R.; Palomaki, P. K. B.; Neale, N. R.; Furtak, T. E.; Beard, M. C. Size-Dependent Exciton Formation Dynamics in Colloidal Silicon Quantum Dots. *ACS Nano* **2016**, *10*, 2316−2323.

(139) Cimpean, C.; Groenewegen, V.; Kuntermann, V.; Sommer, A.; Kryschi, C. Ultrafast Exciton Relaxation Dynamics in Silicon Quantum Dots. *Laser Photon. Rev.* **2009**, *3*, 138−145.

(140) Sykora, M.; Mangolini, L.; Schaller, R. D.; Kortshagen, U.; Jurbergs, D.; Klimov, V. I. Size-Dependent Intrinsic Radiative Decay Rates of Silicon Nanocrystals at Large Confinement Energies. *Phys. Rev. Lett.* **2008**, *100*, 067401.

(141) VandeVondele, J.; Hutter, J. Gaussian Basis Sets for Accurate Calculations on Molecular Systems in Gas and Condensed Phases. *J. Chem. Phys.* **2007**, *127*, 114105.

(142) Goedecker, S.; Teter, M.; Hutter, J. Separable Dual-Space Gaussian Pseudopotentials. *Phys. Rev. B: Condens. Matter Mater. Phys.* **1996**, *54*, 1703−1710.

(143) Hartwigsen, C.; Goedecker, S.; Hutter, J. Relativistic Separable Dual-Space Gaussian Pseudopotentials from H to Rn. *Phys. Rev. B: Condens. Matter Mater. Phys.* **1998**, *58*, 3641−3662.

(144) Krack, M. Pseudopotentials for H to Kr Optimized for Gradient-Corrected Exchange-Correlation Functionals. *Theor. Chem. Acc.* **2005**, *114*, 145−152.

(145) Perdew, J. P.; Burke, K.; Ernzerhof, M. Generalized Gradient Approximation Made Simple. *Phys. Rev. Lett.* **1996**, *77*, 3865−3868.

(146) Grimme, S.; Antony, J.; Ehrlich, S.; Krieg, H. A Consistent and Accurate *Ab Initio* Parametrization of Density Functional Dispersion Correction (DFT-D) for the 94 Elements H-Pu. *J. Chem. Phys.* **2010**, *132*, 154104.

(147) Press, W. H.; Teukolsky, S. A.; Vetterling, W. T.; Flannery, B. P. Numerical Recipes. *The Art of Scientific Computing*, 3rd ed; Cambridge University Press, 2007.

(148) Bussi, G.; Donadio, D.; Parrinello, M. Canonical Sampling through Velocity Rescaling. *J. Chem. Phys.* **2007**, *126*, 014101.

(149) Dasog, M.; Bader, K.; Veinot, J. G. C. Influence of Halides on the Optical Properties of Silicon Quantum Dots. *Chem. Mater.* **2015**, *27*, 1153−1156.

(150) Michalak, D. J.; Amy, S. R.; Aureau, D.; Dai, M.; Estève, A.; Chabal, Y. J. Nanopatterning Si (111) Surfaces as a Selective Surface-Chemistry Route. *Nat. Mater.* **2010**, *9*, 266−271.

(151) Stuhlmann, C.; Bogdányi, G.; Ibach, H. Surface Phonons of the Hydrogen-Terminated Si (111)(1x1) Surface. *Phys. Rev. B: Condens. Matter Mater. Phys.* **1992**, *45*, 6786.

(152) Granucci, G.; Persico, M.; Zoccante, A. Including Quantum Decoherence in Surface Hopping. *J. Chem. Phys.* **2010**, *133*, 134111.

(153) Barnard, A. S.; Wilson, H. F. *Silicon Quantum Dot Data Set.* v2.; CSIRO. Data Collection. (accessed June 8, 2022).

(154) Barnard, A. S.; Wilson, H. F. Optical Emission of Statistical Distributions of Silicon Quantum Dots. *J. Phys. Chem. C* **2015**, *119*, 7969−7977.

(155) Zhang, Q.; Bayliss, S. C. The Correlation of Dimensionality with Emitted Wavelength and Ordering of Freshly Produced Porous Silicon. *J. Appl. Phys.* **1996**, *79*, 1351−1356.

(156) Gabay, D.; Wang, X.; Lomakin, V.; Boag, A.; Jain, M.; Natan, A. Size Dependent Electronic Properties of Silicon Quantum Dots—An Analysis with Hybrid, Screened Hybrid and Local Density Functional Theory. *Comput. Phys. Commun.* **2017**, *221*, 95−101.

(157) Von Behren, J.; Van Buuren, T.; Zacharias, M.; Chimowitz, E. H.; Fauchet, P. M. Quantum Confinement in Nanoscale Silicon: The Correlation of Size with Bandgap and Luminescence. *Solid State Commun.* **1998**, *105*, 317−322.

(158) Plasser, F.; Granucci, G.; Pittner, J.; Barbatti, M.; Persico, M.; Lischka, H. Surface Hopping Dynamics Using a Locally Diabatic Formalism: Charge Transfer in the Ethylene Dimer Cation and Excited State Dynamics in the 2-Pyridone Dimer. *J. Chem. Phys.* **2012**, *137*, 22A514.

(159) Lin, Q.; Li, L.; Liang, S.; Liu, M.; Bi, J.; Wu, L. Efficient Synthesis of Monolayer Carbon Nitride 2D Nanosheet with Tunable Concentration and Enhanced Visible-Light Photocatalytic Activities. *Appl. Catal., B* **2015**, *163*, 135−142.

(160) Shi, A.; Li, H.; Yin, S.; Liu, B.; Zhang, J.; Wang, Y. Effect of Conjugation Degree and Delocalized π-System on the Photocatalytic Activity of Single Layer g-C_3N_4. *Appl. Catal., B* **2017**, *218*, 137−146.

(161) Agrawal, S.; Lin, W.; Prezhdo, O. V.; Trivedi, D. J. Ab Initio Quantum Dynamics of Charge Carriers in Graphitic Carbon Nitride Nanosheets. *J. Chem. Phys.* **2020**, *153*, 054701.

(162) Meek, G. A.; Baczewski, A. D.; Little, D. J.; Levine, B. G. Polaronic Relaxation by Three-Electron Bond Formation in Graphitic Carbon Nitrides. *J. Phys. Chem. C* **2014**, *118*, 4023−4032.

(163) Wang, J.; Cherevan, A. S.; Hannecart, C.; Naghdi, S.; Nandan, S. P.; Gupta, T.; Eder, D. Ti-Based MOFs: New Insights on the Impact of Ligand Composition and Hole Scavengers on Stability, Charge Separation and Photocatalytic Hydrogen Evolution. *Appl. Catal., B* **2021**, *283*, 119626.

(164) Santaclara, J. G.; Olivos-Suarez, A. I.; du Fossé, I.; Houtepen, A.; Hunger, J.; Kapteijn, F.; Gascon, J.; van der Veen, M. A. Harvesting the Photoexcited Holes on a Photocatalytic Proton Reduction Metal−Organic Framework. *Faraday Discuss.* **2017**, *201*, 71−86.